Technical University of Crete

School of Electronic and Computer Engineer

Digital Image and Signal Processing Laboratory

Non-linear Synchronization Methods on

Magnetoencephalographic (MEG) Recordings

Master of Thesis

Marios Antonakakis

Supervisor: **Professor Michalis Zervakis**
School of Electronic and Computer
Technical University of Crete

Chania, September 2015

………………………

Marios Antonakakis

Electronic and Computer Engineer
Technical University of Crete

Credits

Abstract

Cross-frequency coupling (CFC) is thought to represent a basic mechanism of functional integration of neural networks across distant brain regions. Furthermore, several neuroimaging studies have suggested that functional brain connectivity networks exhibit "small-world" characteristics, whereas recent studies based on structural data have proposed a "rich-club" organization of brain networks, whereby nodes of high connection density tend to connect among themselves compared to nodes of lower density. In this study, CFC profiles are analyzed from resting state Magnetoencephalographic (MEG) recordings obtained from 30 mild traumatic brain injury (mTBI) patients and 50 controls. The non-linear synchronization metric, mutual information (MI) is used to quantify the phase-to-amplitude coupling (PAC) of activity among the recording sensors in six nonoverlapping frequency bands. After forming the CFC-based functional connectivity graphs (FCGs), a tensor representation and tensor subspace analysis is employed to identify an set of features with low dimensions for subject classification as mTBI or control. Keeping FCGs from the optimal set of features, an "attack strategy" to is developed to compare the rich-club and small-world organizations and identify the model that describes best the topology of brain connectivity. Results show that the controls form a dense network of stronger local and global connections, indicating higher functional integration compared to mTBI patients. Furthermore, mTBI patients could be separated from controls with more than 90% classification accuracy. Finally, the results suggest that resting state MEG connectivity networks follow a rich-club organization. These findings indicate that the analysis of brain networks computed from resting-state MEG with PAC and tensorial representation of connectivity profiles may provide a valuable biomarker for the diagnosis of mTBI.

Keywords: Magnetoencephalography (MEG); mild traumatic brain injury; cross-frequency coupling, tensors, brain models, attacking strategy

Περίληψη

Η σύζευξη συχνοτήτων (Cross-Frequency Coupling - CFC) θεωρείται ότι αντιπροσωπεύει έναν βασικό μηχανισμό της λειτουργικής ολοκλήρωσης των νευρικών δικτύων στις απόμακρες περιοχές του εγκεφάλου. Επιπρόσθετα, πολλές μελέτες νευροαπεικόνισης έχουν προτείνει ότι τα εγκεφαλικά δίκτυα λειτουργικής συνδεσιμότητας επιδεικνύουν χαρακτηριστικά εγκεφαλικών δικτύων γνωστά ως "small-world", ενώ πρόσφατες μελέτες βασιζόμενες σε διαρθρωτικά δεδομένα έχουν προτείνει μια οργάνωση εγκεφαλικών δικτύων γνωστή ως "rich-club", σύμφωνα με την οποία κόμβοι υψηλής πυκνότητας συνδέσεων τείνουν να συνδέονται μεταξύ τους συγκριτικά με κόμβους χαμηλής πυκνότητας συνδέσεων. Στην παρούσα εργασία, αναλύθηκαν πρότυπα τύπου CFC βασιζόμενοι σε καταγραφές κατάστασης ηρεμίας Μαγνητοεγκεφαλογραφήματος (Magneto-encephalography – MEG) που λήφθηκαν από τριάντα ασθενείς με ήπιες κρανιοεγκεφαλικές κακώσεις (mild traumatic brain injury – mTBI) και πενήντα άτομα χωρίς κανένα πρόβλημα (control). Μέσω του μη-γραμμικού μέτρου αλληλεξαρτώμενου συγχρονισμού της αμοιβαίας πληροφορίας (Mutual Information), έγινε ο υπολογισμός της σύζευξη φάση-πλάτους (phase-amplitude couple –PAC) της δραστηριότητας μεταξύ των αισθητήρων καταγραφής σε έξι μη-επικαλυπτόμενες ζώνες συχνότητας. Μετά την διαμόρφωση των CFC-βασισμένων λειτουργικών γράφων συνδεσιμότητας (functional connectivity graphs -FCGs), υιοθετήθηκε μια τανυστική αντιπροσώπευση και ένας τανυστικός υποχώρος για να προσδιορίσουμε το βέλτιστο σύνολο χαρακτηριστικών γνωρισμάτων για την υπαγόμενη ταξινόμηση ως mTBI ή control. Διατηρώντας μόνο γράφους από ένα σύνολο χαρακτηριστικών γνωρισμάτων μικρών διαστάσεων, αναπτύχθηκε μια «στρατηγική επίθεσης» ώστε να συγκρίνουμε τις εγκεφαλικές οργανώσεις δικτύων, "rich-club"και "small-world", καθώς επίσης και να προσδιοριστεί εκείνο το μοντέλο που περιγράφει καλύτερα την τοπολογία της εγκεφαλικής συνδεσιμότητας. Τα αποτελέσματά μας δείχνουν ότι το σύνολο των κανονικών ατόμων διαμορφώνει ένα πυκνό δίκτυο των ισχυρότερων τοπικών και σφαιρικών συνδέσεων, δείχνοντας υψηλότερη λειτουργική ολοκλήρωση έναντι των ασθενών mTBI. Επιπλέον, οι mTBI ασθενείς μπορούν να χωριστούν από τους κανονικούς ελέγχους με την ακρίβεια ταξινόμησης περισσότερο από 90%. Τέλος, τα αποτελέσματα της παρούσας εργασίας προτείνουν ότι τα δίκτυα συνδεσιμότητας MEG δεδομένων κατάστασης ηρεμίας ακολουθούν οργάνωση "rich-club". Αυτά τα συμπεράσματα δείχνουν ότι η ανάλυση των δικτύων εγκεφάλου που υπολογίζονται σε καταγραφές κατάστασης ηρεμίας MEG με PAC και την τανυστική αντιπροσώπευση των σχεδιαγραμμάτων συνδεσιμότητας μπορεί να παρέχει ένα πολύτιμο δείκτη (λεγόμενο και ως biomarker) για τη διάγνωση του mTBI.

Λέξεις Κλειδιά: Μαγνητοεγκεφαλογράφημα (ΜΕΓ); ήπιες κρανιοεγκεφαλικές κακώσεις; σύζευξη συχνοτήτων; Τανυστής; Εγκεφαλικά μοντέλα; Στρατηγικές επίθεσης

Contents

Table of Contents

Chapter 1.
Introduction

1.1.   Brain

The nervous system is a complex network that communicates with diverse nervous tissues whose function is to transmit information in order to control the bodily activities and functions (Carr and Brown, 2001). It enables the body to detect and react to changes in the environment and to interpret the resulting nervous impulses. Attending to anatomical and physiological criteria, the nervous system can be divided into two systems (Carr and Brown, 2001; National Institute on Aging, 2008):

- Central Nervous System (CNS). It is the largest part of the nervous system. It is contained in the skull and spinal cavity, which protects the brain and the spinal cord, respectively.

- Peripheral Nervous System (PNS). It is composed of the nervous tissue that extends from or arrive at the skull and spinal cavity. The PNS extends through the limbs and the flesh of the torso.
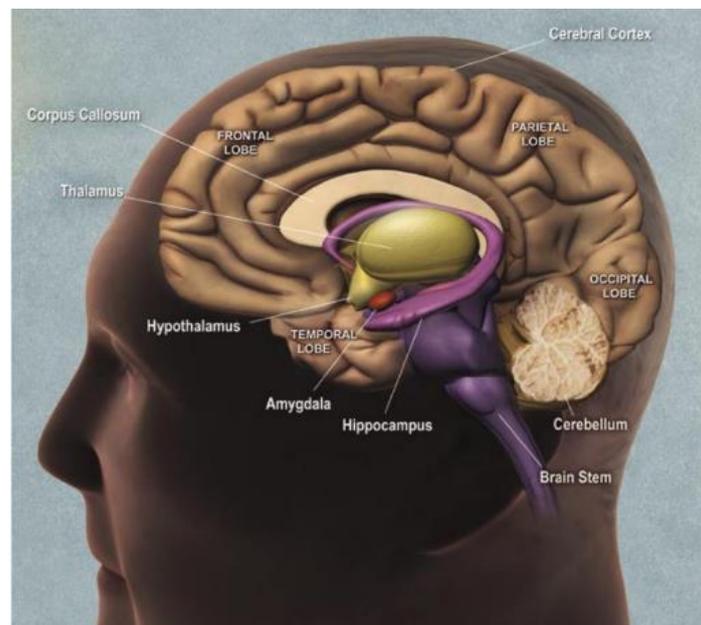
Figure 1. View of the brain showing some of its main parts (National Institute on Aging, 2008).

The brain is the largest part of the CNS. As shown in **Figure 1**, it is composed of several structures, such as the cerebellum lays above the brain stem. The cerebrum is the most evolved part of the brain. It is divided into two cerebral hemispheres connected by nerves at the corpus callosum. The outer layer of the hemispheres is the cortex, which plays a key role in memory, attention, thought, language and other cognitive functions. Attending at the most prominent fissures of the cortex, each hemisphere can be divided into four lobes, each of which has different roles (National Institute on Aging, 2008):

- The frontal lobe, which lays at the front of the brain, controls executive functions like thinking, planning, and problem solving, as well as memory, attention and movement.
- The parietal lobe, which sits behind the frontal lobe, deals with the perception and integration of stimuli from the senses.
- The temporal lobe, which runs along the side of the brain under the frontal and parietal lobes, deals with the senses of smell, taste and sound and the formation and storage of memories.
- The occipital lobe, which is at the back of the brain, is concerned with vision.

In general, the CNS is composed of glial and nerve cells (Sanei and Chambers, 2007). The glial cells are located between neurons, holding them in place and supporting them with nutrients. They also remove damaged cells and other debris and provide insulation to the neurons. However, the transmission and processing of the information in the nervous system is only carried out by the neurons (National Institute on Aging, 2008).

Of note is that the activity recorded in the EEG and MEG is the ultimate result of the transmission of the nerve impulse or action potential. Action potentials are temporary changes in the neuron membrane potential which are transmitted along the axon. They are produced as a result of an exchange of ions across the neuron membrane and the stimulus for their creation is the chemical activity of neurotransmitters at the synapses. The conduction velocity of action potentials ranges from 1 m/s to 100 m/s (Sanei and Chambers, 2007).

1.2.   Electromagnetic Brain Signals and Rhythms

When neurons are activated, the synaptic currents are produced within the dendrites and propagated through the soma and axon. This current generates a magnetic field measurable by MEG equipment and a secondary electrical field over the scalp measurable by EEG equipment. These fields usually lie below 100 Hz (Sanei and Chambers, 2007). However, only when large populations of active neurons are simultaneously active, a sufficiently large signal is generated to be recorded on the scalp (Sanei and Chambers, 2007).

The cortex can generate electromagnetic activity spontaneously. This activity is composed of superimposed rhythms. It must be noticed that, the higher the synchronization of nearby neurons, the larger the amplitude and lower the frequency of the resulting activity. In healthy adults, the amplitudes and frequencies of such signals change from one state of a human to another, such as wakefulness or sleep (Sanei and Chambers, 2007). The characteristics of the waves also change with age. Usually, five major brain waves are distinguished by their frequency range in the brain activity: δ (0.5 Hz –4 Hz), θ (4 Hz – 8 Hz), α (8 Hz – 13 Hz), β (13 Hz – 30 Hz) and γ (over 30 Hz) (Sanei and Chambers, 2007).

The δ activity ranges from about 0.5 Hz to 4 Hz. It is mainly associated with deep sleep but it may also be present in the waking state. Sometimes, this activity may be confused with artefact signals caused by large muscles of the neck and jaw (Sanei and Chambers, 2007).

The θ waves lie within the range of 4 Hz to 8 Hz. They have been linked with access to unconscious material, creative inspiration and deep meditation. The θ wave is often accompanied by other frequencies and seems to be related to the level of arousal. It plays an important role in infancy and childhood. Large amounts of θ activity in the waking adult are abnormal and it may indicate pathological problems (Sanei and Chambers, 2007). It is also remarkable that changes in the θ rhythms are analysed for maturational and emotional studies (Sanei and Chambers, 2007).

The α waves appear in the posterior half of the head. Moreover, they are dominant over the occipital region of the brain. Their frequency lies within the range of 8 Hz to 13 Hz. These waves usually appear as a round or sinusoidal shaped signal (Sanei and Chambers, 2007). This rhythm has been related to both a relaxed awareness without any attention and concentration. Most subjects produce α waves with their eyes closed. For

this reason, it has been argued that it actually is a waiting or scanning pattern produced by the visual regions of the brain. The α activity is greatly reduced by opening the eyes, hearing unfamiliar sounds, anxiety or attention (Sanei and Chambers, 2007).

The β rhythm denotes the brain electromagnetic activity varying between 13 Hz and 30 Hz. It is the usual waking rhythm of the brain associated with active thinking, active attention or solving problems (Sanei and Chambers, 2007). The β activity is found in normal adults, mainly over the frontal and central regions. It may also be enhanced around tumoural regions (Sanei and Chambers, 2007).

The γ range corresponds to frequencies over 30 Hz. The amplitude of this rhythm is very low and its occurrence is rare. However, detection of this activity can be used for confirmation of certain brain diseases (Sanei and Chambers, 2007).

1.3.   Mild traumatic brain injury

Mild traumatic brain injury (mTBI) is the most common cause of brain insult. The mildest form of traumatic brain injury (TBI) is that although it is an acute brain injury any residuals from a concussion are short-lived physiological aberrations without lasting neurological sequelae. In the absence of an enduring neurological deficit, the neuropsychological argument has been made that any post-concussion cognitive or behavioral change in function does not reflect permanent neuropathology (Bigler, 2013). Reasons behind these assumptions are that indisputably the majority of those who experience an mTBI return to pre-injury baseline and resume typical function, at least based on traditional neuropsychological measures (Rohling et al. 2011). Transient perturbation of neuronal physiology seems a likely explanation and fits well with the majority of positive outcomes documented in mTBI research (Bigler, 2013).

Typically, patients experience an initial brief change in mental state or consciousness that is followed by post-concussion symptoms (PCS) (Cassidy et al., 2004), such as headaches, fatigue, and dizziness, which usually emerge on the day of injury and persist for at least the first few days thereafter (Boccaletti et al., 2006). In most patients cognition recovers and PCS resolve within three months. However, up to 25% of patients (Sigurdardottir et al., 2009) suffer residual PCS, long-term impairment and sometimes disability (Levin, 2009), so that efficient identification of alterations due to mTBI becomes particularly important. Several cognitive functions are affected by mTBI, including attention (De Monte et al., 2006; Vanderploeg et al., 2005) working memory (Vanderploeg

et al., 2005), episodic memory (Tsirka et al., 2011), verbal learning (De Monte et al., 2006; Ruff et al., 1989), and visual memory (Levin et al., 1987; Raskin, 2000; Ruff et al., 1989).

Conventional neuroimaging techniques, such as acute magnetic source imaging (MRI) and computed tomography (CT), have limited sensitivity to detecting physiological alterations caused by mTBI (Bigler and Orrison, 2004; Johnston et al., 2001; Kirkwood et al., 2006). Current neuroimaging methods now demonstrate that a subgroup of mTBI patients have more than a transient physiological disruption in neural function showing identifiable underlying neuropathology (Bigler and Maxwell 2012 Kasahara et al. 2012; Kim et al. 2013; Lewine et al. 2007; Lipton et al. 2012; Matthews et al. 2012; Wada et al. 2012). Magnetoencephalography (MEG) on the other hand, is a noninvasive functional imaging technique that measures directly neuronal currents in gray matter with extraordinary (<1 ms) temporal resolution and excellent (2–3 mm) spatial localization accuracy (Leahy et al., 1998). Consequently, during the past several years numerous studies have attempted to develop reliable biomarkers of mTBI based on MEG (see reviews by Jeter et al., 2013 and Huang et al., 2009, 2014). Of particular interest is the analysis of resting-state MEG activity either alone (Luo et al., 2013, Zouridakis et al., 2012; Dimitriadis et al., 2015; Li et al., 2015) or combined with diffusion tensor imaging (DTI) MRI (Huang et al., 2014).

1.4. Cross frequency Coupling

Recent approaches to study brain function view the brain as an intricate network of complex systems with abundant interactions between local and distant areas, having the capacity to combine local specialization (segregation) with global integration (Tononi et al., 1994; Tognoli and Kelso, 2014). Fluctuations of spontaneous activity are strongly synchronized among spatially distributed neuronal subsystems (Contreras and Steriade, 1997; Destexhe et al., 1999), suggesting that processing of stimuli is influenced by the dynamics of coherently active networks. These spatiotemporal patterns involve not only low-frequency activity within the δ (1-4 Hz) band or below (Contreras and Steriade, 1997; Destexhe et al., 1999), but also higher frequencies in the θ (4–8 Hz), α (8–12 Hz), β (13–30 Hz) and γ (>30 Hz) ranges (Steriade et al., 1996a, b; Destexhe et al., 1999). Oscillations in these frequency bands are known to be involved in a variety of cognitive processes (Engel and Fries, 2010; Siegel et al., 2012).

One approach to understanding the dynamic nature of connections between local and distant neural assemblies is the analysis of functional and effective connectivity

(Friston et al., 1994): the former captures patterns of statistical dependence, whereas the latter attempts to extract networks of causal influences of one physiological time series over another (Aertsen et al., 1989). Several studies have demonstrated changes in functional connectivity patterns after brain tumor resection (Douw et al., 2008), recovery from stroke (Gerloff et al., 2006), and traumatic brain injury (Castellanos et al., 2010; Zouridakis et al., 2012) suggesting that functional connectivity graphs (FCGs) of brain activity are sensitive to changes due to brain insult.

The MEG is a complex signal containing components of different frequency interaction. Power spectrum analysis based on Fourier, wavelet, or Gabor transform can uncover amplitude modulations within the above-defined frequencies across time. Intrinsic coupling modes (ICMs) in ongoing activity are thought to reflect the action of two different coupling mechanisms (Engel et al., 2001): one that arises from phase coupling of band-limited oscillatory signals, and another one that results from coupled aperiodic fluctuations of signal envelopes. When studying ICMs, apart from exploring the relationship between same-frequency signals, it is highly interesting to also quantify functional relationships between signals of different frequencies (Jensen and Colgin, 2007; Palva and Palva, 2011; Jirsa and Muller, 2013; Dimitriadis et al., 2014), as this cross-frequency coupling (CFC) has been hypothesized to represent the mechanism for the interaction between local and global processes and therefore it is directly related to the integration of distributed information. The most important components of the CFC is included by

1. **Amplitude** (envelope): instantaneous magnitude of a complex-valued signal. Intuitively, a function that interpolates from peak to peak for an oscillatory waveform.

2. **Frequency** (band): oscillations generated by active neuronal tissue often exhibit characteristic rhythms. Traditionally, neuronal oscillations have been divided into different bands, including slow oscillations (<1 Hz) and delta (1– 4 Hz), theta (4-8 Hz), alpha (8–12 Hz), beta (12–30) and gamma (>30 Hz) bands, with further subdivisions becoming more common. Neuronal oscillation: transient, rhythmic variation in neuronal activity.

3. **Phase**: measure of the position within a full cycle of an oscillatory waveform. Typically measured in radians [–π, π] or degrees [–180, 180]. For example, the peak of a sinusoidal waveform has a phase of 0 radians, whereas the trough has a phase of π radians.

Recently, different forms of cross-frequency interactions were described (Jensen and Colgin, 2007), namely power-to-power, phase-to-phase, phase-to-frequency, and phase-to-power. There is ample evidence that the last type of CFC, also called phase-amplitude modulation, occurs very often in both animals and humans in the prefrontal cortices, the hippocampus, and other distributed cortical areas (Osipova et al., 2008; Tort et al., 2008, 2009, 2010; Cohen et al., 2009a, b; Colgin et al., 2009; Axmacher et al., 2010a, b; Voytek et al., 2010).

The study of phase–amplitude CFC is an emerging area of research, with a diversity of quantitative methods in use. A variety of different measures demonstrating CFC makes it less likely that CFC is due to an artifact inherent to a given analysis method, but can make it difficult to compare results across studies. Here we describe in brief the quantitative methods in current use; interested readers will find detailed mathematical accounts elsewhere (Penny et al., 2008; Tort et al., 2010; Young et al., 2009; Kramer et al., 2008; Cohen, 2008). Tort and colleagues recently compared eight different phase–amplitude measures (Tort et al., 2010). These include:

- The height ratio (HR) (Lakatos et al., 2005), in which high-frequency (HF) amplitude values are binned and averaged as a function of the low-frequency (LF) phase, and the maximum difference in average amplitude values divided by the maximum average amplitude is used as a metric.

- The Kullback-Liebler (KL)-based modulation index (KL-MI) (Tort et al., 2008; 2009). Like the HR measure, this index starts with the average binned HF amplitude as a function of LF phase, and then determines the deviation of this distribution-like function from a uniform distribution using KL divergence.

- The mean vector length modulation index (MVL-MI) (Canolty et al., 2006). This index computes the modulus of the average value of a complex-valued time series in which each sample point has a modulus of the HF amplitude and a phase of the LF phase.

- The envelope–signal correlation (ESC) (Bruns, A. and Eckhorn, R., 2004; Penny et al., 2008). Here the correlation coefficient between the (real-valued) LF filtered signal and the HF amplitude envelope is computed. A normalized envelope– signal correlation (NESC) can be computed using the (realvalued) cosine of the LF phase (to remove LF amplitude information).

- The general linear model (GLM) measure (Penny et al., 2008). This generalization of the NESC measure removes the dependence of CFC detection on the phase of coupling, and can detect CFC for any LF phase.

- The power spectral density (PSD) of the HF amplitude envelope (Cohen, 2008). One advantage of this method is that only the HF is fixed and multiple low frequencies can be examined at once, unlike the methods discussed above.

- The coherence value (CV) (Colgin et al., 2009), for which the coherence spectrum between the HF amplitude envelope and the raw (unfiltered) signal is computed.

- The phase-locking value (PLV) (Penny et al., 2008; Cohen, 2008). Here the HF amplitude is filtered to extract an LF phase, which is then compared with the LF phase extracted from the raw (unfiltered) signal.

- Mutual information (MI) (Voytek et al., 2010; Xu et al., 2013). In order to measure the strength of directional CFC between sensors, the HF amplitude is filtered to extract an LF phase, which is then compared with the LF phase extracted from the raw (unfiltered) signal.

Of these nine measures, no gold standard has yet emerged; each metric has different advantages and disadvantages, depending on the goals of the experimenters. In comprehensive simulation studies, Penny et al. compared four of the above measures (MVL-MI, PLV, ESC, GLM) and found that MVL-MI has the weakest sensitivity of the four under conditions of low signal-to-noise ratio or short data epochs, and recommend use of the GLM metric (Penny et al., 2008). However, as shown by Tort et al., the CV, PLV, ESC, and GLM metrics can only detect the presence or absence of phase-amplitude CFC, and cannot assess the intensity of CFC (Tort et al., 2010), which the KL-MI, MVL-MI, PSD and HR metrics can do. Note, however, that a PSD (or CV) peak is a necessary but not sufficient condition for phase–amplitude CFC; HF activity can exhibit LF amplitude modulations without being phase coupled to LF activity. In general, selection of a metric should be based on experimenter goals, with different metrics proving useful for different purposes.

Distinguishing brain-based phase–amplitude CFC from artifactual coupling is a prime concern. Kramer and colleagues explored possible sources of spurious CFC, focusing on the effects of non-sinusoidal waveforms (Kramer et al., 2008). They demonstrated that phase–phase CFC can be used to detect spurious phase– amplitude

CFC (Kramer et al., 2008). Current study adopts suggestion of Kramer et al. (2008) and through the PAC-MI, quantifies the strength of the directional CFC among the sensors.

Only a few MEG studies have considered CFC interactions at rest or during execution of active tasks. An early study (Osipova et al., 2008) reported that gamma power was phase-locked to alpha activity over occipital brain regions at rest with eyes closed (EC). Interestingly, there was no peak in the gamma activity estimated by Fourier transform, but a clear peak was evident only when studied in relation to the alpha phase. In another MEG study (Palva et al., 2005), cross-frequency of phase synchrony was identified as the main communication mechanism between frequencies from 3 to 80 Hz. In particular, enhanced CFC phase synchrony was revealed between the α, β, and γ frequency bands during a continuous mental arithmetic task. This enhancement of CFC phase synchrony could be attributed to the integration needed among different brain areas activated during the task that were synchronized in the dominant frequency (Palva et al., 2005).

1.5.   Functional connectivity graph compression and discrimination

In general, functional connectivity captures deviations from statistical independence between distributed and often spatially remote neuronal units. Statistical dependence may be estimated by measuring correlation or covariance, spectral coherence or phase-locking. Functional connectivity estimates from any kind of synchronization measure and between every possible pair of EEG or MEG recording sites are employed to form FCGs. Of note, previous brain decoding studies based on FCGs typically treated the obtained FCGs as vectors in a high-dimensional space (Shen et al., 2010; Richardi et al., 2011) and handled in a standard pattern-analytic fashion. The main drawback of this approach is that it overlooks the inherent format of FCGs. In fact, since each FCG has a straightforward tabular representation, it can be considered as a second order tensor. The relationship stored in the corresponding matrix constitutes important features that reflect ordered associations between brain areas, and hence should be faithfully preserved in a low dimensional representation. To this end, we treat FCGs as tensors and employ tensor subspace analysis (TSA) (He et al., 2005) as a suitable and convenient feature extraction strategy in this work.

Although two-way or multi-way tensors have already been used in neuroscience studies for improving classification accuracy (Latchoumane et al., 2012) in most cases the focus was on extracting consistent patterns in frequency domain within a recording

condition or from a population based original multichannel signals (Cichocki et al., 2009; Dimitriadis et al., 2013; Leonardi et al., 2013). To the best of our knowledge, there is only one fMRI study, in which dynamic FCGs were modeled via a group-based 3D-tensorial approach and in an attempt to associate particular connectivity patterns with different brain states (Leornadi et al., 2013). In a preliminary version of this work Dimitriadis et al., (2013) have realized a single-subject study aiming at differentiating deviant workload levels (two levels) based on connectivity patterns recovered from signals recorded over parieto-occipital brain areas. Based on the above promising results, we attempted here to correctly identify the workload levels among five different cognitive states by incorporating estimates of both intra and inter-frequency phase coupling within a single FCG representation.

1.6. Brain-Network Models

With respect to brain-network models, an example of widely shared organizational structure is the small-world (SW) phenomenon, whereby networks are simultaneously highly clustered. It means that there are nodes that are connected to each other are also likely to have many nearest (first degree) neighbors in common and highly efficient (the average path length between a pair of nodes is short) (Watts and Strogatz, 1998; Palva and Palva, 2011; Vértes and Bellmore, 2015). Alternatively, the so-called SW network organization (or model) combines high levels of local clustering among nodes and relatively short paths that link all nodes of a network (Palva and Palva, 2011). Several brain connectivity studies using different neuroimaging modalities, including fMRI, EEG, and MEG, have suggested that functional brain networks exhibit properties of SW network organization (Palva and Palva, 2011; Vértes and Bellmore, 2015; Dimitriadis et al., 2015).

Hubs are also found in almost all complex networks. They can be defined in many ways, but the simplest definition is as high-degree nodes, where the degree of a node is the number of edges that connect it to other nodes in the network. High-degree hub nodes, with many connections to the rest of the network, are more probable in internet, metabolic, social and brain networks than expected in a random graph: the degree distribution is more fat-tailed than it would be for a random graph (Vértes and Bellmore, 2015). Many complex networks share a further related property – the tendency for the hubs to connect to each other to form a rich club (RC) of hub nodes that are densely connected to each other and to the rest of the network (Vértes and Bellmore, 2015). The so-called RC network

organization (or model) provides important information about the top-level structure of a network, its hierarchical ordering and node specialization (van den Heuvell and Sporns, 2011). The RC network organization has been explored in simulations (Senden et al., 2014) and in a diffusion tensor imaging study (van den Heuvell and Sporns, 2011), but it has not been employed yet with EEG or MEG recordings. Therefore, it is not clear whether the RC network organization can provide any features complementary to the SW network organization of FCGs derived from resting state MEG.

Brain networks can be characterized by two models, the SW and RC where the latter has proposed by a few studies to better describe structural data (van den Heuvell and Sporns, 2011). It is important to note that a RC network may also present SW characteristics in a sub-network (Bullmore and Sporns, 2012). To identify the model that describes best the topology of brain connectivity, an "attack strategy" should be adopted (Gallos et al., 2006; van den Heuvell and Sporns, 2011) which is also used for general networks (Gallos et al., 2006). The attack strategy should focus on SW or RC nodes in order to reveal their importance in the information transfer in the whole network.

The role of a node (or a set of nodes) in the level of global efficiency of a network (or network organization such as SW or RC) can be evaluated by examining the damage inflicted by attack on that node, simulated as a decrease in the weights of its connections (van den Heuvell and Sporns, 2011). The current attack strategy was previous used by other authors on diffusion tensor imaging (DTI) (van den Heuvell and Sporns, 2011). The DTI includes thousands of thousands edges and such an attack strategy revealed that hub regions were found to be more densely interconnected than would be expected based solely on their degree, together forming a rich club. Furthermore, Gallos and colleagues (2006) simulated similar to current study attack strategies on scale-free networks. Albert and Barabasi (2002) showed that there are similar to our current attack strategies which are constructed based on global information of the network (i.e. global efficiency).

Two forms of attack can be used: "targeted attack" and "random attack to hub connections." In the targeted attack, we reduce the weights of connections that interconnect RC and SW nodes. In the random attack, we reduce the weights of the connections between RC and SW nodes. Therefore, a network can be described as SW or RC network observing the reduction of the level of the initial global efficiency during an attack simulation because a global efficiency reduction means that important network nodes are affected by "attacks".

In general, the RC can be seen as a variation of SW network organization, with different topological features (Mišić et al., 2014). There are many research studies that support the SW network organization of brain networks (Palva and Palva, 2011; Dimitriadis et al., 2015), but there has been recent evidence suggesting that RC model is also met in the brain-network topology (van den Heuvell and Sporns, 2011; Mišić et al., 2014; Bullmore and Sporns, 2012). In particular, SW network organization characterizes a network (or a local region of it) if any node can communicate with any other node over a few 'hops'. Alternatively, the RC network organization reflects the network structure where hub nodes have disproportionately dense interconnections and high number of shortest paths (van den Heuvell and Sporns, 2011; Mišić et al., 2014; Bullmore and Sporns, 2012), so that connections among RC nodes carry more traffic than SW nodes (Mišić et al., 2014).

The SW and RC network organizations play a significant role in order to investigate how the brain network is affected by diseases such as Schizophrenia, Alzheimer or Autism. A comparison of SW network organization between control and SZ brain networks demonstrated that the SZ group presented lower global efficiency for both of models (Liu et al., 2008; Rubinov et al., 2009). However, other studies (van den Heuvel and Kahn, 2011; Fornito et al., 2012; van den Heuvel et al., 2013) revealed differences in SZ and control groups using RC network organization showing that RC network organization between high-degree hub nodes was significantly affected in patients, together with a reduced density of rich club connections. In addition, regarding Alzheimer and Autism, the affection of the RC and SW core of the brain has more global effects on brain communication and thereby affect multiple cognitive domains (see the review of Bullmore and Sporns, 2012).

1.7. Aims and innovation of current study

Current thesis aims to investigate whenever spontaneous MEG activity through CFC patterns and advance signal processing, machine learning and graph theory aspects reveal an appropriate biomarker for mTBI. In particular, it scopes to demonstrate how the phase of low frequency spontaneous MEG activity modulates higher frequency activity in mTBI subjects (Florin and Bairrat, 2015). Then, by adopting a phase-to-amplitude coupling (PAC) estimator using the non-linear metric MI (Xu et al., 2013) to quantify the strength of directional CFC between pairs of frequencies, it constructs cross-frequency

FCGs in mTBI patients and controls. It hypothesizes that PAC at rest can capture intrinsic network interactions that play a crucial role in information exchange and integration. It examines the proposition that mTBI can affect functional integration, mainly the communication between different cell assemblies that function on a prominent frequency, and these functional changes of intrinsic networks can be captured by CFC. Furthermore, assuming that brain injuries affect the information flow within the brain network, it attempts to compare both SW and RC models in revealing which model dominates to the averaged FCGs of both groups. In particular, we introduce a common framework that allows the comparison of the RC organization against the SW based on CFC estimates. It adopts a general attacking strategy (Gallos et al., 2006; van den Heuvell and Sporns, 2011) on RC and SW nodes and random nodes in order to estimate the degree of damage on the global efficiency (GE) of the network (van den Heuvell and Sporns, 2011). It hypothesizes that the percentage of GE reduction after "attack" can reveal the organization that describes best FCGs computed from CFC estimates (van den Heuvell and Sporns, 2011). The developed methodology is validated using resting-state MEG data obtained from 50 neurologically intact controls, and 30 individuals with mild traumatic brain injury (mTBI) (Zouridakis et al. 2012).

1.8. The structure of current study

The Thesis is organized into three major chapters as follows. Chapter 2 presents the details of methods used in the current study. It describes the MEG recordings, the preprocessing steps for artifact detection and elimination, the dimensionality reduction algorithm and the classification schemes. In addition, several methods (Global and Local Efficiency or Physical distances between PAC and Sensors) are discussed for the comparison of the CFC couples between two groups. Two different network organizations and a general attack strategy are adopted in order to reveal which organization of CFC couples dominates the average FCG of each group. Chapter 3 presents the results of our study, the performance of each classification scheme on the current dataset and examines differences between the two groups as potential biomarkers. Furthermore, it demonstrates the network organization that dominates the dataset. Chapter 4 discusses the current findings and compares current results with other studies. It summarizes the findings and provides concluding remarks in order to indicate if the used metric (i.e. CFC) is an appropriate biomarker in the case of mTBI and suggests future analysis directions.

Chapter 2.
Amplitude-to-Phase Coupling

2.1. Summary of Chapter

Our study employs network analysis of filtered directed graphs that are constructed from interacting networks coupled at specific frequency pairs and quantify local and global connection density in both subject groups. Cross-frequency coupling (CFC) is thought to represent a basic mechanism of functional integration of neural networks across distant brain regions. In the present study, we measure the basic type of CFC called phase-to-amplitude (PAC). We first formed functional connectivity graphs based on PAC measure which then be explored for topological differences between the two groups and for their community profile. An important step to understand topological differences is to first estimate a basic network structure with global (functional integration) and local efficiency (functional segregation) at both network and sensor levels and then detect consistent group-functional clusters (Rubinov and Sporns, 2010). CFC is a key mechanism of brain functionality with which two distant brain areas oscillating on their prominent frequency can communicate straightforward and quickly. To investigate how relationship of physical distance between sensors with the corresponding PAC strength in control group and how it was affected in mTBI subjects (Kolchinsky et al., 2014), we illustrated the distribution of PAC strength over physical distance between the sensors. To further understand how changes of decreased local CFC correlate with possible underlying lesioned areas and if these are effects of main injury site or global effects where the entire brain sustained injury, we calculate patterns of intra-hemispheric CFC asymmetry and anterior-posterior anisotropy. Previous studies showed a reduction in frontal and hemispheric asymmetry in TBI patients using PET (Reuter-Lorenz et al., 2000; Levine et al., 2002, correspondingly). We demonstrate group differences related to the lateralization of functional strength over a hemisphere and examine the predominance of functional strength anteriorly or posteriorly.

2.2. Subjects and recording procedure

The present study is part of a larger mTBI project (Levin, 2009) supported by the Department of Defense (DoD). mTBI was defined using the guidelines of DoD (Assistant Secretary, 2007) and the American Congress of Rehabilitation Medicine (Kay et al., 1993). The project was approved by the Institutional Review Boards (IRBs) at the participating institutions and the Human Research Protection Official's review of research protocols for DoD. All procedures were compliant with the Health Insurance Portability and Accountability Act (HIPAA).

Thirty right-handed mTBI patients (30.05 ± 9.41 years of age; 17 men and 13 women) were recruited from three trauma centers in the greater Houston metropolitan area that participated in the larger study (Levin, 2009). The Galveston Orientation and Amnesia Test (GOAT) (Levin et al., 1979) was administered prior to obtaining informed consent to identify cognitive impairment that would preclude provision of informed consent. Inclusion criteria required the presence of a head injury occurring within the preceding 24 hours, Glasgow Coma Scale (GCS, Teasdale & Jennett, 1974) score 13-15, loss of consciousness <30 minutes including 0 minutes, post-traumatic amnesia <24 hours including 0 minutes, and a negative head CT scan. Exclusion criteria included a score on the Abbreviated Injury Scale (AIS) >3 for any body part, previous head injury requiring hospitalization, history of significant pre-existing disease, such as psychotic disorder, bipolar disorder, post-traumatic stress disorder (PTSD), past treatment for alcohol dependence or substance abuse, blood alcohol level >80 mg/dL at the time of consent, documentation of intoxication, left-handedness, and contraindications for MRI, including claustrophobia and pregnancy. Details about the demographics of the mTBI are shown in Appendix A.

The control group included fifty right-handed age- and gender-matched normal subjects (29.2 ± 9.1 years of age) drawn from a normative data repository at UTHSC-Houston. Previous head injury, history of neurologic or psychiatric disorder, substance abuse, and extensive dental work and implants incompatible with MEG was exclusion criteria for the control subjects. The research protocol received institutional approval prior to the study.

Subjects were asked to lie on a bed as still as possible with eyes closed. Approximately 5 minutes of resting-state MEG activity was recorded from each subject using a 248-channel whole-head Magnes WH3600 system (4D Neuroimaging Inc., San

Diego, CA). Data were collected at a sampling rate of 1017.25 Hz and bandpass filtered in hardware between 0.1–200 Hz. Axial gradiometer recordings were transformed to planar gradiometer field approximations using the *sincos* method implemented in MATLAB Toolbox Fieldtrip (Oostenveld et al., 2011).

2.3. Data preprocessing

The MEG data underwent artifact reduction using Matlab (The MathWorks, Inc., Natick, MA, USA) and Fieldtrip (Oostenveld et al., 2011). Filtering with a notch filter at 60 Hzwas used to reduce the effects of line noise and it was followed by independent component analysis (ICA) to separate cerebral from non-cerebral activity using the extended Infomax algorithm as implemented in EEGLAB (Delorme and Makeig, 2004). The data were also whitened and reduced in dimensionality using principal component analysis with a threshold set to 95% of the total variance (Delorme and Makeig, 2004; Escudero et al., 2011; Antonakakis et al., 2013). The statistical values of kurtosis, Rényi entropy, and skewness of each independent component were used to eliminate ocular and cardiac artifacts. A component was considered an artifact if more than 20% of its values after normalization to zero mean and unit variance were outside the range [-2, +2] (Escudero et al., 2011; Dimitriadis et al., 2013b; Antonakakis et al., 2013).

2.4. Estimation and Classification of Amplitude-to-Phase Coupling

2.4.1 Estimation of Amplitude-to-Phase Coupling

We explored cross-frequency interactions using phase-to-amplitude coupling (PAC), whereby the phase of a low-frequency rhythm modulated the amplitude of a higher-frequency oscillation (Tort et al., 2008; Voytek et al., 2010; Xu et al., 2013). PAC was calculated between sensors X_i, X_j $(i, j = 1 \ldots 248)$ of a multidimensional array of time series X using mutual information (MI), a nonlinear metric that measures the interdependence of the two time series X_i and X_j. The MI concept stems from information theory and offers several advantages: it is sensitive to any type of dependence between the time series including nonlinear relations and generalized synchronization; it is relatively robust to outliers, and it is measured in bits, a physically meaningful unit.

Initially, data from all sensors were filtered in several frequency bands, namely $\delta(0.5 - 4\text{Hz}), \theta(4 - 8\text{Hz}), \alpha(8 - 15\text{Hz}), \beta(15 - 30\text{Hz}), \gamma_1(30 - 45\text{Hz}),$ and $\gamma_2(45 - 80\text{Hz})$. Then, to compute the PAC values we used the Hilbert Transform (HT) to estimate the phase $(\varphi_{f,i})$ and amplitude $(A_{f,i})$ of every filtered time series $X_{f,i}$, separately in each frequency band using

$$\varphi_{f,i} = \tan^{-1}\left(\frac{Im\left(HT(X_{f,i})\right)}{Re\left(HT(X_{f,i})\right)}\right) \text{ (1)}$$

and

$$A_{f,i} = \left|\sqrt{Im\big(HT(X_{f,i})\big)^2 + Re\big(HT(X_{f,i})\big)^2}\right| \text{ (2)}$$

where $Im(HT(X_{f,i}))$ and $Re\big(HT(X_{f,i})\big)$ are the imaginary and real part of $HT(X_{f,i})$, respectively. We then applied a band-pass filter to $A_{f,i}$ using the same filter parameters used to extract $X_{fl,i}$, giving a new time series, $A_{fh,fl,i}$. A second Hilbert transform was then used to extract the phases of the f_l-filtered $f_{h(high)}$ amplitude envelope $(\varphi_{fh,fl,i})$ (Voytek et al., 2010).

According to the above, the mathematical definition of MI for the estimation of PAC between the phase of low frequency $f_l, \varphi_{f_l,i}$, and the amplitude of the high frequency $f_h, \varphi_{fh,f_l,i}$, between two sensors X_i and X_j, is given by

$$PAC_{f_l, f_h}(i,j) = I\big(\varphi_{f_l,i}; \varphi_{fh,f_l,i}\big) = \sum_{y \in Y}\sum_{x \in X} p(x,y)\log\left(\frac{p(x,y)}{p_x(x)p_y(y)}\right)\text{(3)}$$

where $X = \varphi_{f_l,i}$ and $Y = \varphi_{fh,f_l,i}$, and $p(x,y)$ is the joint probability distribution function of X and Y, respectively, and $p_x(x) = \sum_{y \in Y} p(x,y)$ and $p_y(y) = \sum_{x \in X} p(x,y)$ are the marginal probability distribution functions of X and Y, respectively (Tsiaras et al., 2011).

2.4.2   Significant links

The aforementioned procedures result in a matrix of PAC values between the time series on all possible pairs of sensors that is modeled as a fully connected, directed, weighted, and symmetric FCG, representing causal influences among all cortical regions. The maximum number of possible directed connections N in a network with k=248nodes is $N = k^2$=61504, and the FCG is extremely dense. Therefore, the FCG connections must be filtered out so that the pattern with the most significant connections can emerge. We performed two kinds of filtering: topological filtering based on graph theory principles and data-driven thresholding.

Topological filtering relies on graph-based analysis (Bullmore and Sporns, 2009; Bassett et al., 2009; He and Evans, 2010; Stam, 2010; Dimitriadis et al., 2014), which is used to capture the structure of the neural system under investigation and the relationship between separation and integration of neural populations. Small-word structures are characterized by a dense network of local connections and a limited number of long-range connections that provide efficient communication between distant nodes. Efficiency in information transmission between nodes is measured as the inverse of the shortest distance between the nodes, while the average of all pair-wise efficiencies represents the global efficiency of the graph. The function cost relates to the energy expenditure needed for a network to maintain its efficiency, and it is given by the ratio of existing connections divided by the total number of possible pairwise connections in a network. Global cost efficiency (GCE) is defined as the global efficiency GE at a given cost C minus the cost ($GE-C$), which typically has a positive maximum value at some cost C_{max}, for an economical small-world network. Importantly, this metric of network topology is independent of arbitrary, investigator-specified thresholds. Instead, the cost efficiency curve is estimated over a wide range of thresholds, and the behavior of the curve is summarized by its maximum value, which occurs at a data driven connection density or cost C (Bassett et al., 2009). ***Figure 2*** illustrates an example of how the edges, the GCE function and the GE are changed when the threshold C changes of graph for a control subject and the δ-β frequency. Following those statistical filtering aspects in order to identify significant links, we applied a data-driven thresholding scheme based on maximization of global cost-efficiency as a function of network cost.
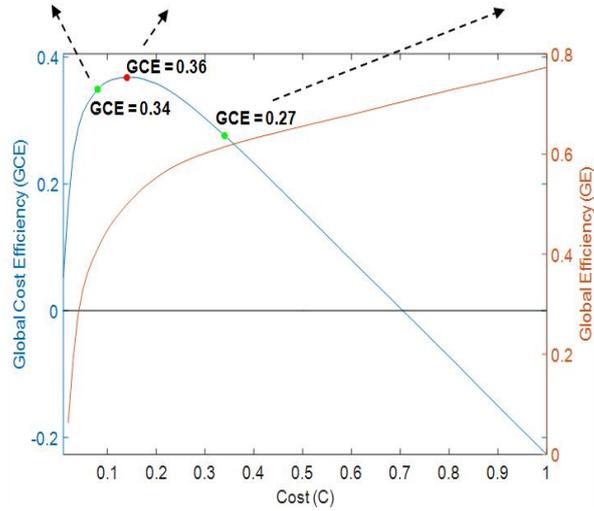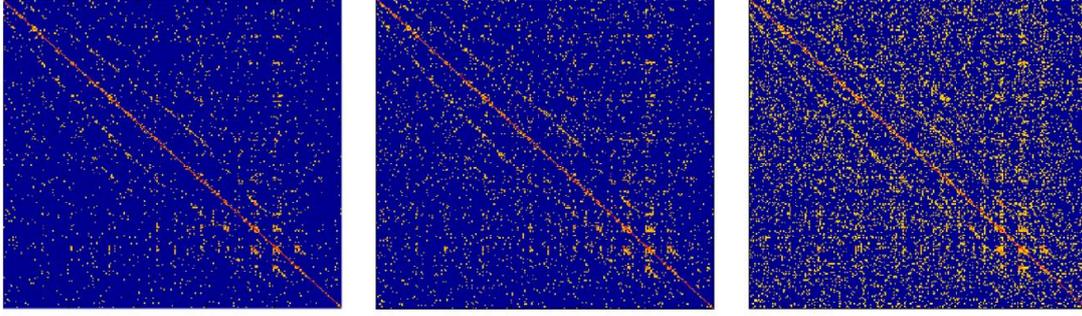
Figure 2. Global cost efficiency as a function of network cost. Three examples of graphs with significant links for the δ-β frequency pair from a control subject. The red dot corresponds to the maximum value (optimal threshold) of global cost efficiency while the green dots represent non-optimal thresholds.

2.4.3   Classification of FCG patterns

The values of the PAC matrices are considered features in a high-dimensional space that can be used to classify the FCGs obtained from individual subjects. In most studies, however, FCGs are treated as vectors in a high-dimensional space (e.g. Shen et al.,2010; Pollolini et al., 2010; Richiardi et al., 2011), an approach that disregards the inherent tabular representation of FCGs and their nature as second-order tensors. To overcome this limitation, we treat FCGs as tensors and resort to tensor subspace analysis (TSA) for appropriate feature extraction (He and Cai, 2005). In our formulation, the tensor form was given as (subjects x sensors x sensors) (Dimitriadis et al., 2013a; 2014).

The TSA procedure blends multi-linear algebra and manifold data learning. Given some FCGs sampled from the space of functional connectivity patterns, the TSA approximation is modeled by first building an adjacency graph capturing the proximity relationships among the connectivity patterns and then deriving a tensor subspace that faithfully represents these relationships. TSA provides an optimal linear approximation to the FCG manifold.

36

2.4.3.1. TSA learning of FCG patterns

2.4.3.1.1. Linear Dimensionality Reduction in Tensor Space

The generic problem of linear dimensionality reduction in the second order space is the following. Given a set of tensors (i.e. matrices) $X_1, \ldots, X_m \in R^{n_1} \otimes R^{n_2}$ (where X be a $n_1 \times n_2$ FCG) find two transformation matrices U of size $n_1 \times k_1$ and V of $n_2 \times k_2$ that maps these m tensors to a set of tensors $Y_1, \ldots, Y_m \in R^{k_1} \otimes R^{n_2}$, such that Y_i "represents" X_i, where $Y_i = U^T X_i V$. The method is of particular interest in the special case where $X_1, \ldots, X_m \in M$ and M is a nonlinear sub-manifold embedded in $R^{n_1} \otimes R^{n_2}$.

2.4.3.1.2. Optimal Linear Embedding

The "true" domain of FCGs most probably forms a nonlinear sub-manifold embedded in the ambient space of 2nd order tensors. We attempt to find a linear subspace approximation to the sub-manifold in the sense of local isometry using an adopted TSA. The adopted technique is actually the tensorial counterpart of Locality Preserving Projection (LPP).

Given a set of m tensors $X_{i=1:m}$, with each one being the tabular version of a single-trial FCG and having associated the cognitive load level as class label, TSA starts by building an $m \times m$ weight-matrix S that represents the nearest neighbour graph G among the tensors. In our implementation, the element S_{ij} was set as

$$S_{ij} = \begin{cases} \exp\left(-\dfrac{\|X_i - X_j\|^2}{t}\right) & \text{condition}^1 \\ 0 & \text{otherwise} \end{cases} \quad (4)$$

where t is a control-parameter usually referred as "radius of influence" and condition states that X_i, X_j should share the same class label and anyone of them is among the kk-nearest neighbors of the other; the functional in (4) is known as heat kernel (here is employed with frobenius norm). The frobenius norm is defined as $\|X\|_F = \sqrt{\sum_{i=1}^{m} \sum_{j=1}^{m} |X_{ij}|^2}$.

Then TSA seeks two transformation matrices U and V, such that when applied to each tensor to result in a mapping that would preserve the neighborhood relations encoded in G. Mathematically is formulated in the form of the below objective function:

$$\min_{U,V} \sum_{ij} \left\| U^T X_i V - U^T X_j V \right\|^2 S_{ij} \quad (5)$$

that incurs a heavy penalty if neighboring tensors X_i and X_j of the same class are mapped far apart. By denoting with D the diagonal matrix with elements $D_{ii} = \sum_j S_{ij}$, the above optimization problem is reformulated as two coupled problems of eigenvector analysis:

$$(D_U - S_U)\mathrm{v} = \lambda D_U \mathrm{v}$$
$$D_U = \sum_i D_{ii} X_i^T U U^T X_i, \qquad (6)$$
$$S_U = \sum_{ij} S_{ij} X_i^T U U^T X_j$$

$$(D_V - S_V)\mathrm{u} = \lambda D_\mathrm{v} \mathrm{u}$$
$$D_V = \sum_i D_{ii} X_i V V^T X_i^T, \qquad (7)$$
$$S_V = \sum_{ij} S_{ij} X_i V V^T X_j^T$$

The optimal U and V can be obtained by iteratively computing the generalized eigenvectors of (7) and (8) as it presented by the below detailed pseudo algorithmic steps. However, it is difficult to simultaneously compute the optimal U and V since the matrixes D_V, S_V, D_U, and S_U are not fixed. Both U and V were iteratively compute as follows. We first fix U then V can be computed by solving the Eq. (7). Once V is obtained, U can be updated by solving the Eq. (8). The optimal U and V can then be obtained by iteratively computing the generalized eigenvectors of (7) and (8). Matrices $D_U, D_V, D_U - S_U$, and $D_V - S_V$ are all symmetric and positive semi-definite.

In the present study, the dimensionality of the reduced tensors (i.e. the numbers of eigenvectors for the mapping $Y_i = U^T X_i V$) was optimized, via cross-validation, for each subject independently so as to achieve the highest classification performance. The numbers of neighbors and the heat parameter were set in a similar way.

- **Pseudo algorithmic steps of the TSA**

Input: A set of N sample matrices (FCGs) $\{X_i\}_{i=1}^{N}$ with class label information

Define the diagonal matrix $D = diag(d_1, d_2, ..., d_N)$ with $d_i = \sum_{j=1}^{N} S_{ij}$.

Output: left and right transformation matrices U and V

    (1) Initialize U with an identity matrix;

    (2) Until convergence Do:

        (2.1) Form the matrix $M_D^{(U)} = (D_U - S_U)$;

        (2.2) Form the matrix $M_L^{(U)} = D_U$;

        (2.3) Compute the l_2 eigenvectors $\{v_i\}_{i=1}^{l_2}$ of the pencil $\left(M_D^{(U)}, M_L^{(U)}\right)$

        corresponding to the largest l_2 eigenvalues;

        (2.4) Set $V = \left[v_1, v_2, ..., v_{l_2}\right]$;

        (2.5) Form the matrix $M_D^{(V)} = (D_V - S_V)$;

        (2.6) Form the matrix $M_L^{(V)} = D_V$;

        (2.7) Compute the l_1 eigenvectors $\{u_i\}_{i=1}^{l_1}$ of the pencil $\left(M_D^{(V)}, M_L^{(V)}\right)$;

        (2.8) Set $U = \left[u_1, u_2, ..., u_{l_1}\right]$;

    End Do

2.4.3.2.   Learning machines for classification

Classification of FCGs from individual subjects starts by computing the TSA representation and is followed by comparison with FCGs of known label. In our study, we used the k-NN algorithm and the Frobenius norm (Horn and Johnson, 1990) as measure of similarity. Apart from this classification scheme, indicated as "TSA+k-NN", we also employed TSA with ensemble classification ("TSA+ENS") and TSA with extreme learning machine (ELM) classification ("TSA+ELM").

2.4.3.2.1.   K-nearest neighbor

K-nearest-neighbor (kNN) classification is one of the most fundamental and simple classification methods and should be one of the first choices for a classification study when there is little or no prior knowledge about the distribution of the data. It was developed from the need to perform discriminant analysis when reliable parametric estimates of probability densities are unknown or difficult to determine. Moreover, it is commonly based on the Euclidean distance between a test sample and the specified training samples. Let x_i be an input sample with p features $x_{i1}, x_{i2}, ..., x_{ip}, n$ be the total number of input

samples $(i = 1, 2, \ldots, n)$ and p the total number of features $(j = 1, 2, \ldots, p)$. The Euclidean distance between sample x_i and x_l $(l = 1, 2, \ldots, n)$ is defined as

$$d(x_i, x_l) = \sqrt{(x_{i1} - x_{l1})^2 + (x_{i2} - x_{l2})^2 + \cdots + \left(x_{ip} - x_{lp}\right)^2}. \textbf{(8)}$$

A graphic depiction of the nearest neighbor concept is illustrated in the Voronoi tessellation (Voronoi, 1907) shown in **_Figure 3_**. The tessellation shows 19 samples marked with a "+", and the Voronoi cell, R, surrounding each sample. A Voronoi cell encapsulates all neighboring points that are nearest to each sample and is defined as

$$R_i = \left\{x \in R_p : d(x, x_i) \leq d(x, x_m), \forall i \neq m\right\}, \textbf{(9)}$$

where R_i is the Voronoi cell for sample x_i, and **x** represents all possible points within Voronoi cell R_i. Voronoi tessellations primarily reflect two characteristics of a coordinate system: i) all possible points within a sample's Voronoi cell are the nearest neighboring points for that sample, and ii) for any sample, the nearest sample is determined by the closest Voronoi cell edge. Using the latter characteristic, the k-nearest-neighbor classification rule is to assign to a test sample the majority category label of its k nearest training samples. In practice, k is usually chosen to be odd, so as to avoid ties. The $k = 1$ rule is generally called the nearest-neighbor classification rule.

Classification typically involves partitioning samples into training and testing categories. Let x_i be a training sample and x be a test sample, and let ω be the true class of a training sample and $\widehat{\omega}$ be the predicted class for a test sample $(\omega, \widehat{\omega} = 1, 2, \ldots, \Omega)$. Here, Ω is the total number of classes.

During the training process, we use only the true class ω of each training sample to train the classifier, while during testing we predict the class $\widehat{\omega}$ of each test sample. It warrants noting that kNN is a "supervised" classification method in that it uses the class labels of the training data. Unsupervised classification methods, or "clustering" methods, on the other hand, do not employ the class labels of the training data.
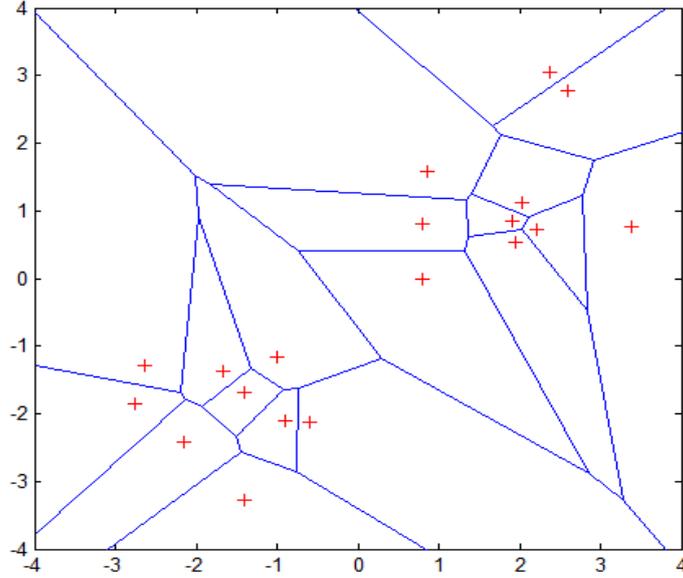
Figure 3. Voronoi tessellation showing Voronoi cells of 19 samples marked with a "+".

With 1-nearest neighbor rule, the predicted class of test sample **x** is set equal to the true class ω of its nearest neighbor, where $\boldsymbol{m_i}$ is a nearest neighbor to **x** if the distance

$$d(m_i, x) = \min_j\{d(m_j, x)\} \ (\mathbf{10})$$

For k-nearest neighbors, the predicted class of test sample **x** is set equal to the most frequent true class among k nearest training samples. This forms the decision rule $D: x \rightarrow \widehat{\omega}$.

The confusion matrix used for tabulating test sample class predictions during testing is denoted as C and has dimensions $\Omega \times \Omega$. During testing, if the predicted class of test sample x is correct (i.e., $\widehat{\omega} = \omega$), then the diagonal element $c_{\omega\omega}$ of the confusion matrix is incremented by 1. However, if the predicted class is incorrect (i.e., $\widehat{\omega} \neq \omega$), then the off-diagonal element $c_{\widehat{\omega}\omega}$ is incremented by 1. Once all the test samples have been classified, the classification accuracy is based on the ratio of the number of correctly classified samples to the total number of samples classified, given in the form

$$Acc = \frac{\sum_{\omega}^{\Omega} c_{\omega\omega}}{n_{total}} \ (\mathbf{11})$$

where $c_{\omega\omega}$ is a diagonal element of C and n_{total} is the total number of samples classified.

Consider a machine learning study to classify 19 samples with 2 features, X and Y. **Table 1** lists the pairwise Euclidean distance between the 19 samples. Assume that sample x_{11} is being used as a test sample while all remaining samples are used for training. For k=4, the four samples closest to sample x_{11} are sample x_{10} (blue class label), sample x_{12} (red class label), x_{13} (red class label), and x_{14} (red class label).

Table 1. Euclidean distance matrix D listing all possible pairwise Euclidean distances between 19 samples.

	x_1	x_2	x_3	x_4	x_5	x_6	x_7	x_8	x_9	x_{10}	x_{11}	x_{12}	x_{13}	x_{14}	x_{15}	x_{16}	x_{17}	x_{18}
x_2	1.5																	
x_3	1.4	1.6																
x_4	1.6	1.4	1.3															
x_5	1.7	1.4	1.5	1.5														
x_6	1.3	1.4	1.4	1.5	1.4													
x_7	1.6	1.3	1.4	1.4	1.5	1.8												
x_8	1.5	1.4	1.6	1.3	1.7	1.6	1.4											
x_9	1.4	1.3	1.4	1.5	1.2	1.4	1.3	1.5										
x_{10}	2.3	2.4	2.5	2.3	2.6	2.7	2.8	2.7	3.1									
x_{11}	2.9	2.8	2.9	3.0	2.9	3.1	2.9	3.1	3.0	1.5								
x_{12}	3.2	3.3	3.2	3.1	3.3	3.4	3.3	3.4	3.5	3.3	1.6							
x_{13}	3.3	3.4	3.2	3.2	3.3	3.4	3.2	3.3	3.5	3.6	1.4	1.7						
x_{14}	3.4	3.2	3.5	3.4	3.7	3.5	3.6	3.3	3.5	3.6	1.5	1.8	0.5					
x_{15}	4.2	4.1	4.1	4.1	4.1	4.1	4.1	4.1	4.1	4.1	1.7	1.6	0.3	0.5				
x_{16}	4.1	4.1	4.1	4.1	4.1	4.1	4.1	4.1	4.1	4.1	1.6	1.5	0.4	0.5	0.4			
x_{17}	5.9	6.2	6.2	5.8	6.1	6.0	6.1	5.9	5.8	6.0	2.3	2.3	2.5	2.3	2.4	2.5		
x_{18}	6.1	6.3	6.2	5.8	6.1	6.0	6.1	5.9	5.8	6.0	3.1	2.7	2.6	2.3	2.5	2.6	3.0	
x_{19}	6.0	6.1	6.2	5.8	6.1	6.0	6.1	5.9	5.8	6.0	3.0	2.9	2.7	2.4	2.5	2.8	3.1	0.4

2.4.3.2.2. Ensemble Classification

Ensemble learning is an effective technique that has increasingly been adopted to combine multiple learning algorithms to improve overall prediction accuracy (Dietterich et al., 2000). Subspace ensembles also have the advantage of using less memory than ensembles with all predictors, and can handle missing values. The random subspace ensemble classifiers perform relatively inferior to other ensemble classifiers (Ho, 1998; Bertoni et al., 2005; Kuncheva et al., 2010). *Random subspace* method has been used for linear classifiers as nearest neighbor (Skurichina, 2002). These group of ensemble methods are particularly useful for high-dimensional datasets (as in our case) because increased classification accuracy can be achieved by generating multiple prediction models each with a different feature subset (Bertoni et al., 2005; Kuncheva et al., 2010). The basic random subspace algorithm performs the following steps:

1. Choose without replacement a random set of *m* predictors from the *d* possible values.

2. Train a weak learner using just the *m* chosen predictors.

3. Repeat steps 1 and 2 until there are *n* weak learners.

4. Predict by taking an average of the score prediction of the weak learners, and classify the category with the highest average score.

Using an implantation delivered by ensemble classification toolbox of MATLAB (The MathWorks, Inc., Natick, MA, USA), the ensemble classification of the random space method evaluated using with 5 predictors per learner and totally 20 learners according to the lowest cross-validated error in the ensemble which was the smallest number that gave high classification performance.

2.4.3.2.3. Extreme Learning Machine

During the past years, extreme learning machine (ELM) (Huang et al., 2006; 2012) has been becoming an increasingly significant research topic for machine learning and artificial intelligence, due to its unique characteristics, i.e., extremely fast training, good generalization, and universal approximation/classification capability. ELM is an effective solution for the single hidden layer feedforward networks (SLFNs), and has been demonstrated to have excellent learning accuracy/speed in various applications, such as face classification (Mohammed et al., 2011), image segmentation (Pan et al., 2012), and human action recognition (Minhas et al., 2010).

ELM is as an emerging learning technique provides efficient unified solutions to generalized feed-forward networks including but not limited to (both single- and multi-hidden-layer) neural networks. ELM theory (Huang et al., 2006) showed that hidden neurons are important but can be randomly generated and independent from applications, and that ELMs have both universal approximation and classification capabilities. ELM selected in the classification scheme due to its computational elegancy and fast-learning capabilities, which lead to competitive performance with respect to other contemporary learning algorithms like back propagation neural networks (BPNNs), radial basis function networks (RBFNs) and support vector machines (SVMs) (Kim et al., 2009).

Suppose that SLFNs with *L* hidden nodes can be represented by the following equation:

$$f_L(\mathrm{x}) = \sum_{i=1}^{L} G_i(\mathrm{x}, \mathbf{a}_i, b_i) \cdot \beta_i, \qquad \mathbf{a}_i \,\epsilon\, \mathbf{R}^d, b_i, \beta_i \epsilon \mathbf{R} \quad \textbf{(12)}$$

where $G_i(\cdot)$ denotes the ith hidden node activation function, $\mathbf{a}_i$ is the input weight vector connecting the input layer to the ith hidden layer, b_i is the bias weight of the ith hidden layer, and β_i is the output weight. For additive nodes with activation function g, G_i is defined as follows:

$$G_i(\mathrm{x}, \mathbf{a}_i, b_i) = g(\mathbf{a}_i \cdot \mathrm{x} + b_i) \quad \textbf{(13)}$$

and for radial basis function (RBF) nodes with activation function g, G_i is defined as

$$G_i(\mathrm{x}, \mathbf{a}_i, b_i) = g(b_i \| \mathrm{x} - \mathbf{a}_i \|) \quad \textbf{(14)}$$

Huang et al. (2006) have proved that the SLFNs are able to approximate any continuous target functions over any compact subset $X \,\epsilon\, \mathbf{R}^d$ with above random initialized adaptive or RBF nodes. Let $L_2(X)$ be a space of functions f on a compact subset X in the d-dimensional Euclidean space $\mathbf{R}^d$ such that $|f|^2$ is integrable, that is, $\int X\, |f(x)|^2 dx < \infty$. For $u, v \in L_2(X)$, the inner product $\langle u, v \rangle$ is defined by

$$\int_X u(\mathrm{x}) v(\mathrm{x})\, dx . \quad \textbf{(15)}$$

The norm in $L_2(X)$ space is denoted as $\| \cdot \|$, and the closeness between network function f_n and the target function f is measured by the $L_2(X)$ distance

$$\|f_L - f\| = \left(\int_X f_n(\mathrm{x}) - f(\mathrm{x}) dx \right)^2 . \quad \textbf{(16)}$$

Theorem 1: Given any bounded non-constant piecewise continuous function $g \colon \mathbf{R} \to \mathbf{R}$, if span $\{ G(\mathbf{a}, b, \mathrm{x}) : (\mathbf{a}, b) \epsilon\, \mathbf{R}^d \times \mathbf{R} \}$ is dense in L^2, for any target function f and any function sequence $g_L(\mathrm{x}) = G(\mathbf{a}_L, b_L, x)$ randomly generated based on any continuous

sampling distribution, $\lim_{n\to\infty} ||f - f_n|| = 0$ holds with probability one if the output weights b_i are determined by ordinary least square to minimize $\left\| f(\mathrm{x}) - \sum_{i=1}^{L} \beta_i g_i(\mathrm{x}) \right\|$.

The theorem above (Huang et al., 2006; Huang and Chen, 2007; 2008)] shows that randomly generated networks with the outputs being solved by least mean square are able to maintain the universal approximation capability, if and only if the activation function g is non-constant piecewise and span $\{G(a, b, x) : (a, b) \in \mathbf{R}^d \times \mathbf{R}\}$ is dense in L^2.

Based on this theorem, ELM can be established for fast learning. Moreover, According to the Theorem 1, the ELM can be built with randomly initialized hidden nodes. Given a training set $\{(x_i, t_i)|x_i \in \mathbf{R}^d, t_i \in \mathbf{R}^m, i = 1, \ldots, N\}$, where x_i is the training data vector, t_i represents the target of each sample, and L denotes the number of hidden nodes. From the learning point of view, unlike traditional learning algorithms (see the related works referred to in Huang, 2014), ELM theory aims to reach the smallest training error but also the smallest norm of output weights (Huang et al., 2006; 2014)

$$\text{Minimize: } \|\beta\|_u^{\sigma_1} + \lambda \|\mathbf{H}\beta - \mathrm{T}\|_v^{\sigma_2} \quad \textbf{(17)}$$

where $\sigma_1 > 0, \sigma_2 > 2, u, v = 0, \left(\frac{1}{2}\right), 1, 2, \ldots + \infty$, $\mathbf{H}$ is the hidden layer output matrix (randomized matrix)

$$H = \begin{bmatrix} h(\mathrm{x}_1) \\ \vdots \\ h(\mathrm{x}_N) \end{bmatrix} = \begin{bmatrix} h_1(\mathrm{x}_1) & \cdots & h_L(\mathrm{x}_1) \\ \vdots & \ddots & \vdots \\ h_1(\mathrm{x}_N) & \cdots & h_L(\mathrm{x}_N) \end{bmatrix} \quad \textbf{(18)}$$

$$\mathbf{T} = \begin{bmatrix} t_1^T \\ \vdots \\ t_N^T \end{bmatrix} = \begin{bmatrix} t_{11} & \cdots & t_{1m} \\ \vdots & \ddots & \vdots \\ t_{N1} & \cdots & t_{Nm} \end{bmatrix} \quad \textbf{(19)}$$

The ELM training algorithm can be summarized as follows (Huang et al., 2012).

1) Randomly assign the hidden node parameters, e.g., the input weights $\mathbf{a}_i$, and biases b_i for additive hidden nodes, $i = 1, \ldots, L$.
2) Calculate the hidden layer output matrix H.
3) Obtain the output weight vector

$$\beta = \mathbf{H}^\dagger \mathbf{T} \quad \textbf{(20)}$$

where $\mathbf{T} = [t_1, \dots, t_N]^T$, $H^\dagger$ is the Moore-Penrose generalized inverse matrix of $\mathbf{H}$.

The orthogonal projection method can be efficiently used for the calculation of MP inverse: $\mathbf{H}^\dagger = (\mathbf{H}^T\mathbf{H})^{-1}\mathbf{H}^T$, if $\mathbf{H}^T\mathbf{H}$ is nonsingular; or $\mathbf{H}^\dagger = (\mathbf{H}^T\mathbf{H})^{-1}$, if $\mathbf{H}\mathbf{H}^T$ is nonsingular. According to the ridge regression theory, it was suggested that a positive value $(1/\lambda)$ is added to the diagonal of $\mathbf{H}^T\mathbf{H}$ or $\mathbf{H}\mathbf{H}^T$ in the calculation of the output weights β. By doing so, according to (Huang et al., 2012) and (Huang et al., 2014), the resultant solution is equivalent to the ELM optimization solution with $\sigma_1 = \sigma_2 = u = v = 2$, which is more stable and has better generalization performance. That is, in order to improve the stability of ELM, we can have

$$\beta = \mathbf{H}^T \left(\frac{1}{\lambda} + \mathbf{H}\mathbf{H}^T \right)^{-1} \mathbf{T} \quad (21)$$

and the corresponding output function of ELM is

$$f(\mathrm{x}) = h(\mathrm{x})\beta = h(x)\mathbf{H}^T \left(\frac{1}{\lambda} + \mathbf{H}\mathbf{H}^T \right) \mathbf{T} \quad (22)$$

or we can have

$$\beta = \left(\frac{1}{\lambda} + \mathbf{H}\mathbf{H}^T \right)^{-1} \mathbf{H}^T\mathbf{T} \quad (23)$$

and the corresponding output function of ELM is

$$f(\mathrm{x}) = h(\mathrm{x})\beta = h(x) \left(\frac{1}{\lambda} + \mathbf{H}\mathbf{H}^T \right)^{-1} \mathbf{H}^T\mathbf{T} \; . \quad (24)$$

2.4.3.3. Feature transformation

Increased performance of a classifier can sometimes be achieved when the feature values are transformed prior to classification analysis. A commonly used feature transformation is standardization.

Standardization removes scale effects caused by use of features with different measurement scales. For example, if one feature is based on patient weight in units of kg and another feature is based on blood protein values in units of ng/dL in the range [-3,3],

then patient weight will have a much greater influence on the distance between samples and may bias the performance of the classifier. Standardization transforms raw feature values into z-scores using the mean and standard deviation of a feature values over all input samples, given by the relationship

$$z_{ij} = \frac{x_{ij} - \mu_j}{\sigma_j} \ (25)$$

where x_{ij} is the value for the i_{th} sample and j_{th} feature, μ_j is the average of all x_{ij} for feature j, σ_j is the standard deviation of all x_{ij} over all input samples. If the feature values take on a Gaussian distribution, then the histogram of z-scores will represent a standard normal distribution having a mean of zero and variance of unity. Once standardization is performed on a set of features, the range and scale of the z-scores should be similar, providing the distributions of raw feature values are alike.

2.4.3.4. Performance assessment with cross-validation

To evaluate the performance of our strategy, a cross-validation scheme was followed. The entire set of individual FCGs (control and mTBI) was randomly partitioned into two subsets, a *training set* (the database of FCGs of known class) corresponding to 80% of the subjects (45 controls and 27 mTBI patients) and a *test set* (subjects for which the class had to be predicted) corresponding to the remaining 20% of the subjects (5 controls and 3 mTBI patients). As a measure of performance we used the correct recognition rate (CC%) calculated as the proportion of subjects in the test set for which the correct label was predicted. The cross-validation scheme was repeated 100 times and the mean value and standard deviation of the overall performance, sensitivity, and specificity were estimated.

2.4.3.5. Statistical measures of the performance of the classification test

The classic statistical measures, accuracy, sensitivity and specificity, evaluate the performance for each of the above classification schemes. The control labels are defined as positives, whereas the mTBI labels as negatives and as a result, the classification performance is demonstrated by

- **Accuracy** $= \dfrac{TP+TN}{TP + FP + FN + TN}$

- **Sensitivity** $= \dfrac{TP}{TP + FN}$ (or the true positive rate) measures the proportion of positives that are correctly identified.

- **Specificity** $= \dfrac{TN}{TN + FP}$ (or the true negative rate) measures the proportion of negatives that are correctly identified.

Where true positive (TP) counts the control labels that were correctly identified, false positive (FP) the mTBI labels that were classified as control, true negative (TN) the mTBI labels that were identified correctly and false negative (FN) the control labels that were classified as mTBI.

2.4.4 Tests of Statistical Analysis

Statistical analysis was performed to detect significant differences between the two groups at every sensor and frequency pair. We developed a sequential methodology for the estimation of the null hypothesis of equal means between the two groups.

First, the single-sample Kolmogorov-Smirnov goodness-of-fit hypothesis test with Lilliefors correction (Conover, 1980) was employed as a test for normality to help select the appropriate type of statistical test to use (parametric t-test or non-parametric U-test). The one-sample Kolmogorov-Smirnov test is a nonparametric test of the null hypothesis that the population cdf of the data is equal to the hypothesized cdf. The two-sided test for "unequal" cdf functions tests the null hypothesis against the alternative that the population cdf of the data is not equal to the hypothesized cdf. The test statistic is the maximum absolute difference between the empirical cdf calculated from x and the hypothesized cdf:

$$D^* = \max_x\left(\left|\hat{F}(x) - G(x)\right|\right) \text{ (26)}$$

where $\hat{F}(x)$ is the empirical cdf and $G(x)$ is the cdf of the hypothesized distribution. The one-sided test for a "larger" cdf function tests the null hypothesis against the alternative that the population cdf of the data is greater than the hypothesized cdf. The test statistic is the maximum amount by which the empirical cdf calculated from x exceeds the hypothesized cdf:

$$D^* = \max_x\left(\hat{F}(x) - G(x)\right) \text{ (27)}$$

The one-sided test for a "smaller" cdf function tests the null hypothesis against the alternative that the population cdf of the data is less than the hypothesized cdf. The test statistic is the maximum amount by which the hypothesized cdf exceeds the empirical cdf calculated from x:

$$D^* = \max_x \left(G(x) - \hat{F}(x) \right) \ (28)$$

If the p-value of the normality test was under the significant level, the non-parametric Mann-Whitney U-test (Gibbons and Chakraborti, 2011) was used; otherwise, a two-sample t-test was employed. The threshold for significance of the *p*-value was set to 95%.

The Mann-Whitney U-test. The Mann-Whitney U-test is a nonparametric test for equality of population medians of two independent samples X and Y. The Mann-Whitney U-test statistic, U, is the number of times a y precedes an x in an ordered arrangement of the elements in the two independent samples X and Y. It is related to the Wilcoxon rank sum statistic in the following way: If X is a sample of size n_x, then

$$U = W - \frac{n_x(n_x - 1)}{2} \ (29)$$

The t-test was performed with either equal or unequal variances depending on a chi-square test (F-test) for heteroscedasticity of the samples. The two-sample t-test is a parametric test that compares the location parameter of two independent data samples. The test statistic is

$$t = \frac{\bar{x} - \bar{y}}{\sqrt{\frac{s_x^2}{n} + \frac{s_y^2}{m}}} \ (30)$$

where $\bar{x}$ and $\bar{y}$ are the sample means, s_x and s_y are the sample standard deviations, and n and m are the sample sizes. In the case where it is assumed that the two data samples are from populations with equal variances, the test statistic under the null hypothesis has Student's t distribution with n + m − 2 degrees of freedom, and the sample standard deviations are replaced by the pooled standard deviation

$$s = \sqrt{\frac{(n-1)s_x^2 + (m-1)s_y^2}{n+m-2}} \quad \textbf{(31)}$$

2.4.5   Elements from Graph Theory

2.4.5.1.   Topological properties of the underlying brain networks

The filtered FCGs were characterized based on the well-known topological metrics of *global* and *local efficiency*, established for weighted graphs and defined below, with N representing the total number of nodes in the network, E the total number of edges, and w_{ij} the weights between nodes.

Global efficiency (GE) for a network W of NxN nodes is the inverse of the harmonic mean of the shortest path length between each pair of nodes and reflects the overall efficiency of parallel information transfer in the network (Achard and Bullmore, 2007; Latora and Marchiori, 2001).

$$GE = \frac{1}{N} \sum_{i \in N} \frac{\sum_{j \in N, j \neq i} (d_{ij})^{-1}}{N - 1} \quad \textbf{(32)}$$

Local efficiency (LE) is understood as a measure of fault tolerance of the network, since it indicates how well the subgraphs exchange information when a particular node is eliminated (Achard and Bullmore, 2007). Specifically, each node is assigned the shortest path length within its subgraph G_i

$$LE = \frac{1}{N} \sum_{i \in N} nodal_{LE_i} = \frac{1}{N} \sum_{i \in N} \frac{\sum_{j,h \in G_i, j,h \neq i} (d_{jh})^{-1}}{k_i(k_i - 1)} \quad \textbf{(33)}$$

where k_i corresponds to the total number of spatial (first level) neighbors of the i-th node, while d denotes the shortest path length.

A low-dimensional representation was used to visualize possible differences between control and mTBI subjects. First, GE and LE values were estimated using the Minkowski

distance ($d_{st} = \sqrt[p]{\sum_{j=1}^{N} |X_{sj} - X_{tj}|^p}$ with p being a positive scalar) and the final estimates were tabulated in an 80 x 80 matrix, since the total number of subjects was 80. Then, using multidimensional scaling (Borg & Groenen, 2005), a well-known dimensionality reduction technique, we were able to project the original multidimensional data in three dimensions. To enhance our understanding about nodal LE, we focused on the δ-β and δ-γ₁ pairs. A single entry of this matrix presents an estimation of the distinction between two different nodal LE profiles. The lower its value, the more alike the segregation pattern between the two subjects.

2.4.5.2.   Consensus community detection in brain networks

Most of the currently available community-detection methods are not deterministic and their results typically depend on initial random seeds, initial conditions, and tie-break rules adopted for their operation. An example of a non-deterministic algorithm is the adopted Louvain method (Blondel et al., 2008). The Louvain method has also been to shown to be very accurate by focusing on ad-hoc networks with known community structure. Moreover, due to its hierarchical structure, which is reminiscent of renormalization methods, it allows to look at communities at different resolutions.

The quality of the partitions resulting from these methods is often measured by the so-called *modularity* of the partition. The modularity of a partition is a scalar value between -1 and 1 that measures the density of links inside communities as compared to links between communities (Girvan and Newman, 2002; Newman, 2006). In the case of weighted networks (weighted networks are networks that have weights on their links, such as the number of communications between two mobile phone users), it is defined as

$$Q = \frac{1}{2m} \sum_{i,j} \left[A_{ij} - \frac{k_i k_j}{2m} \right] \delta(c_i, c_j) \quad \text{(34)}$$

where A_{ij} represents the weight of the edge between i and j, $k_i = \sum_j A_{ij}$ is the sum of the weights of the edges attached to vertex i, c_i is the community to which vertex i is assigned, the δ -function δ(u,v) is 1 if u = v and 0 otherwise and $m = \frac{1}{2} \sum_{ij} A_{ij}$.

The method consists of **two** phases (***Figure 4***). First, it looks for "small" communities by optimizing modularity in a local way. Second, it aggregates nodes of the

same community and builds a new network whose nodes are the communities. These steps are repeated iteratively until a maximum of modularity is attained.
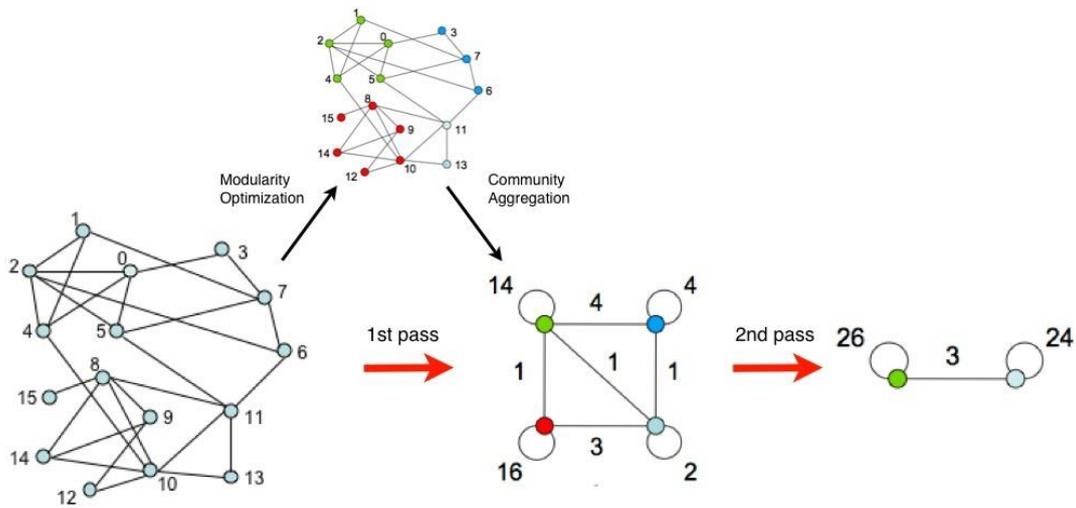
Figure 4. A graphical example of how the Louvain works (Blondel et al., 2008). Reprinted by permission from Journal of Statistical Mechanics: Theory and Experiment 2008 (10), P10008 (12pp). Copyright 2008.

The output of the method therefore gives several partitions. The partition found after the first step typically consists of many communities of small sizes. At subsequent steps, larger and larger communities are found due to the aggregation mechanism. This process naturally leads to hierarchical decomposition of the network. This is obviously an approximate method and nothing ensures that the global maximum of modularity is attained, but several tests have confirmed that our algorithm has an excellent accuracy and often provides a decomposition in communities that has a modularity that is close to optimality.

Consensus clustering is usually employed in network analysis to generate stable results out of partitions generated by a high number of runs of the same stochastic method (Lancichinetti and Fortunato, 2012). The following highlight the algorithmic steps applied in order to identify stable clusterings across the groups.

1) Apply the Louvain method on each group-averaged FCG graph (Bassett et al., 2006).

2) Compute the group consensus matrix D, where D_{ij} is the number of partitions in which vertices i and j of the FCG graph are assigned to the same cluster across iterations and subjects S, divided by S.

3) Repeated steps 1 and 2.

4) Estimate the distance of the D matrix between 1st and 2nd iterations based on the variation of information (VI) metric (Meila, 2007; Dimitriadis et al., 2009, 2012a, b). Suppose we have two partitions X and Y of a set A into disjoint subsets, namely $X = \{X_1, X_2, ..., X_k\}, Y = \{Y_1, Y_2, ..., Y_l\}$. Let $n = \sum_i |X_i| = \sum_j |Y_j| = |A|, p_i = \frac{|X_i|}{n}, q_j = \frac{|Y_j|}{n}, r_{ij} = \frac{|X_i \cap Y_j|}{n}$. Then the variation of information between the two partitions is:

$$VI(X;Y) = -\sum_{i,j} r_{ij} \left[log\left(\frac{r_{ij}}{p_i}\right) + log\left(\frac{r_{ij}}{q_j}\right) \right]. \ (35)$$

This is equivalent to the shared information distance between the random variables i and j with respect to the uniform probability measure on A defined by $\mu(B) := \frac{|B|}{n}$ for $B \subseteq A$. The variation of information satisfies

$$VI(X;Y) = H(X) + H(Y) - 2I(X,Y). \ (36)$$

where $H(X)$ is the entropy of X, and $I(X,Y)$ is mutual information between X and Y with respect to the uniform probability measure on A. A value of 0 denotes similar partitions, while higher values of VI indicate that the distance between the clusters has increased.

If the VI value at iteration t is less than 0.005, then stop and present the clustering of group consensus matrix D. Otherwise, go back to Step 1 for the next iteration.

2.4.5.3.   Physical distance of sensors and PAC strength

To illustrate how the strength of PAC interactions varies as a function of the physical Euclidean distance between MEG sensors, the mean value of CFC-MI between pairs of MEG sensors was plotted for different distance ranges (Kolchinsky et al., 2014). We selected $n_{bins} = 50$ equal-width bins for binning the connectivity distances. The below steps describe the calculation of the physical distance of sensors and PAC strength

1) Computation of the Euclidean distance between each couple of sensors (matrix $D_{anatomical}$ in cm) and between the CFC couples for each frequency couple (matrix $D_{functional}$).

2) Computation of the 2D histogram (Heat-Map) between anatomical distances ($D_{anatomical}$) and functional connectivity strength ($D_{functional}$).

   a. Find the non-zero values of functional strength on $D_{anatomical}$ and $D_{functional}$ using the non-zero indexes of the $D_{functional}$

   b. Sum the non-zero values of the $D_{functional}$ for which $x_{bin} \leq D_{anatomical} \leq x_{bin} + step$, where $step = \max(D_{anatomical}) / n_{bins}$ and $x_{bin} = 0 \dots n_{bins}$

   c. Get the average for each bin in the Heat-Map

Computation of the 1D histograms between the functional connectivity strength ($D_{functional}$).

2.4.5.4.   Intra-Hemispheric Cross Frequency Functional-Coupling Asymmetry and anterior-posterior anisotropy in mTBI

Possible asymmetries between the left (L) and right (R) hemisphere inter-dependencies based on the estimated FCGs on each frequency couple were investigated by defining the following functional-coupling asymmetry index (FAI):

$$FAI = \frac{FC_L - FC_R}{FC_L} \quad (\mathbf{37})$$

where FC_L / FC_R is the aggregate weight from all the connection-strengths among the FCG nodes restricted in either the left or right hemisphere.

Functional connectivity anisotropies between anterior and posterior brain areas based on the estimated FCGs on each frequency pair were investigated by defining the following anterior-posterior asymmetry index (API):

$$API = \frac{FC_{ant} - FC_{post}}{FC_{ant}} \quad (\mathbf{38})$$

where FC_{ant} / FC_{post} is the aggregate weight from all the connection strengths among the FCG nodes restricted in either the left-right frontal areas or left-right parieto-occipital areas. Both subareas consisted of 58 sensors.

2.5. Relative Power

2.5.1 Estimation of Relative Power

The first measure is the computation of the relative power (RP) to analyze the spectral content of MEG recordings in order to reveal differences between two groups. This measure represents the relative contribution of several oscillatory components to the global power spectrum. In comparison with absolute power, RP provides independent thresholds from the recording equipment and lower inter-subject variability (Leuchter et al., 1993, Rodriguez et al., 1999). RP is computed at every sensor in the conventional frequency bands: δ band (1–4 Hz), RP(δ); θ band (4–8 Hz), RP(θ); α band (8–15 Hz), RP(α); β band (15–30 Hz), RP(β); and γ band (30–60 Hz), RP(γ).

Group differences were estimated with Wilcoxon Rank-sum test (U-test; it is described in the above sections) in every frequency band (p < 0.0001, Bonferroni corrected – p' < p/248).

2.5.2 Discrimination of Relative Power

Laplacian score (LS) is a novel feature selection algorithm, based on the idea to evaluate features according to their locality preserving power (Laskaris et al., 2013), that belongs to "filter" methods. Considering vectorial measurements $X_{[N \cdot x \cdot p]} = [x_1|x_2| \dots |x_N]$, associated with $\Lambda = [\lambda_1, \lambda_2, \dots, \lambda_N,]$ class labels, it summarizes the computations involved in the Laplacian score L_r of the r_{th} feature within the following three steps.

1. Construct a nearest neighbor graph G over the N nodes. We put an edge between nodes i and j if they share the same label and x_i is among the k nearest neighbors of x_j (or vice versa). We have set k to 5% of the total number of vectors.

2. Build the $[N \times N]$ weight matrix S such that $S_{ij} = \exp(- \|x_i - x_j\|^2 /t)$ if nodes i and j are connected and $S_{ij} = 0$ otherwise. The parameter t can be thought of as a 'radius of influence' and has been set to the 10% of the average inter-node euclidean distance.

3. The Laplacian score of the r_{th} feature, is computed as follows:

$$\widetilde{\mathbf{f}}_\mathbf{r} = \mathbf{f}_\mathbf{r} - \frac{\mathbf{f}_\mathbf{r}^\mathbf{T}\mathbf{D}\mathbf{l}}{\mathbf{l}^\mathbf{T}\mathbf{D}\mathbf{l}}, \qquad \mathbf{L}_\mathbf{r} = \frac{\mathbf{f}_\mathbf{r}^\mathbf{T}\mathbf{L}\widetilde{\mathbf{f}}_\mathbf{r}}{\widetilde{\mathbf{f}}_\mathbf{r}^\mathbf{T}\mathbf{D}\widetilde{\mathbf{f}}_\mathbf{r}}, \quad (39)$$

with $\mathbf{f_r} = [X_{1r}, X_{2r}, \dots, X_{Nr}]$, $\mathbf{D} = \mathrm{diag}(\mathbf{Sl})$, $\mathbf{l} = [l, \dots, l]^\mathbf{T}$, and $\mathbf{L} = \mathbf{D} - S$ the *graph Laplacian.*

Adopting Laplacian score (LS) as a feature extraction algorithm (Laskaris et al., 2013) and a cross-validation scheme as it is described in the below sections, we attempted to estimate the classification of two groups based on RPs. At every fold of the 5-fold cross-validation, we re-estimated the LS_{Fr_S} of each of the 5 x 248 RPs — frequency bands (Fr) x sensors (S) — and employed a bootstrapping technique by randomizing the labels assigned to each feature for 100.000 times. At each run, a LS_{Fr_S} was estimated for each of the 5 x 248 RPs which finally ended to a null distribution of $LS_{Fr_S}^R$ obtained for every feature (5 x 248 RPs). Next, it was tested whether each the LS_{Fr_S} of each feature deviated from the random and a (one-sided) p-value was assigned as the percentage of $LS_{Fr_S}^R$ that exceeded the original estimated LS_{Fr_S}. Then, the obtained p-values were Bonferroni-corrected (p' < 0.05/(5*248)). Finally, we adopted a k-nearest neighbor (k-NN) classifier.

Chapter 3.
Brain Network Models

Brain networks can be characterized by two network organization, the SW and RC where the latter have proposed by a few studies to better describe structural data (van den Heuvell and Sporns, 2011). It is important to note that a RC network may also presents also present SW characteristics in a sub-network (Bullmore and Sporns, 2012). To identify the model that describes best the topology of brain connectivity, an "attack strategy" should be adopted (Gallos et al., 2006; van den Heuvell and Sporns, 2011) which is also used for general networks (Gallos et al., 2006).

The SW and RC models were constructed only for the averaged FCGs across all subjects, separately for control and mTBI group in order to preserve only the most significant connectivity patterns and only for frequency couple (δ,β). In particular, getting the initial FCGs for the frequency couple (δ,β), we perform a topological filtering (**Chapter 2:** 2.4.2 **Significant links**) on the sensor links on the averaged FCGs across all subjects, separately for the control and mTBI group.

Delta-beta oscillations is an important couple because mTBI injury is associated with an increase in delta, beta bands power (Rapp et al., 2015). Furthermore, delta frequency activity also supports the synchronization of faster frequencies (i.e. beta or gamma) among multiple localized assemblies via CFC (Canolty and Knight, 2010). Delta-beta oscillations varies as a function of state anxiety and approach-avoidance-related motivation. Changes in the association between delta-beta oscillations can be observed following successful psychotherapy (Schutter et al., 2012; Rapp et al., 2015).

3.1. Summary of Chapter

Several neuroimaging studies have suggested that functional brain connectivity networks exhibit "small-world" characteristics, whereas recent studies based on structural data have proposed a "rich-club" organization of brain networks, whereby hubs of high connection density tend to connect among themselves compared to nodes of lower density. In this study, we adopted an "attack strategy" to compare the rich-club and small-world organizations and identify the model that describes best the topology of brain

connectivity. We hypothesized that the highest reduction in global efficiency caused by a targeted attack on each model's hubs would reveal the organization that better describes the topology of the underlying brain networks. We applied this approach to magnetoencephalographic data obtained at rest from neurologically intact controls and mild traumatic brain injury patients. Functional connectivity networks were computed using phase-to-amplitude cross-frequency coupling between the δ and β frequency bands.

3.2. Small World Estimation

Small world is a network that shows a level of clustering higher than that observed in random networks and an average shortest path length that is equal to that observed in random networks (van den Heuvell and Sporns, 2013). An example of SW network organization is presented by **Figure 5**. The computational model of small-world networks proposed by Watts and Strogatz (1998) began by connecting nodes with their nearest neighbors, producing a regular graph that had a high clustering coefficient – C and a high average path length – L. With a probability P, edges were then randomly rewired. When P was equal to unity, all edges were randomly rewired, and thus the network was perfectly random, having a short average path length and clustering coefficient. However, when P was between 0 and 1, there existed some dense local clustering, characteristic of regular networks, and some long-range connections, characteristic of random networks (i.e., the resultant graph was a small-world network with high clustering and low path length).
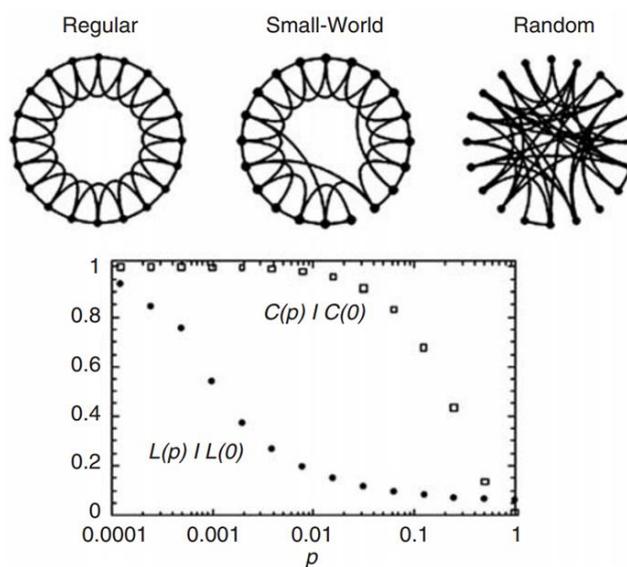
Figure 5. Small-world diagram (Watts and Strogatz 1998). Reprinted by permission from Macmillan Publishers Ltd: Nature 1998; 393:440–2. Copyright 1998.

In our study we estimate the SW network organization based on weighed directed global efficiency (GE), and weighed directed local efficiency (LE) values. A SW network organization reaches a GE value less than a random network, while its LE is higher compared to a random network. The calculation of GE_{RAND} and LE_{RAND} for the random network is based on a permutation procedure (Dimitriadis et al., 2015) that preserves the out-strength but not the in-strength distribution. We repeated this procedure 1000 times and averaged across all random networks to obtain GE_{RAND} and LE_{RAND}. Dimensions of GE_{RAND} and LE_{RAND} are 248x1000. The SW network organization indices $\gamma = LE/LE_{RAND}$ and $\lambda = GE/GE_{RAND}$ are then calculated for the FCG under study and the ratio S, $S_{ratio} = \gamma/\lambda$ is derived. This ratio is greater than 1 in SW networks (Dimitriadis et al., 2015). SW nodes are detected using $S_{ratio} > S_{ration}^{avg} + S_{ration}^{SD}$ where S_{ration}^{avg} is the mean value and S_{ration}^{SD} is the standard deviation across all sensors.

3.3. Rich Club Estimation

Rich-club organization: the propensity of a set of high-degree nodes in a network to be more densely interconnected than expected on the basis of their node degree alone. An example of an RC network organization is presented by **Figure 6**. Network modules linked by sparsely interconnected hubs, which, with the addition of high-cost inter-module connections, form a dense rich club. The rich club consists of five nodes with a degree of four or higher.
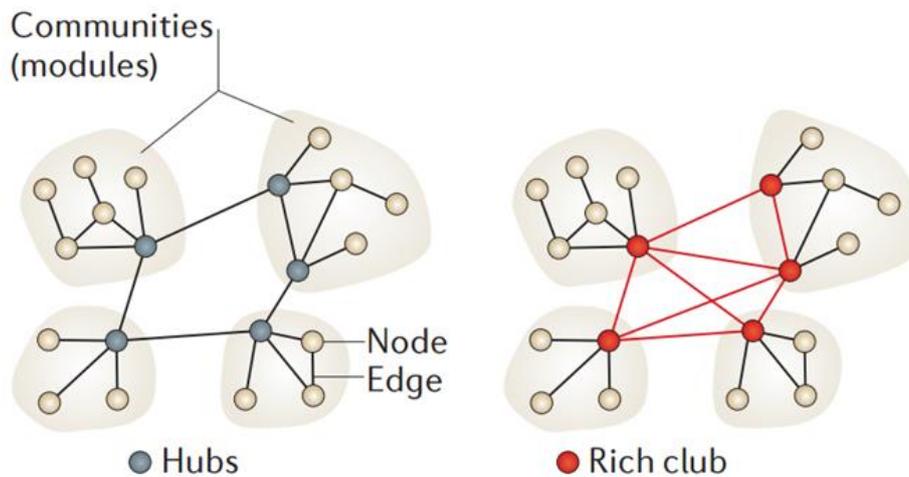
Figure 6. Rich club diagram (Bullmore and Sporns, 2012). Reprinted by permission from Macmillan Publishers Ltd: Nature 2012; 13:336–9. Copyright 2012.

To estimate the RC nodes in the FCGs, the degree k of each node is computed first, which is given by the numbers of in-going and out-going connections on that node. For each value of k, the subset of nodes with degree larger than k is selected. Using this subset, which consists of n nodes and the corresponding $E_{>k}$ connections, the total sum of weights $W_{>k}$ is determined for all edges, where the edge-weights are defined as the number of streamlines (network density) of each edge (van den Heuvell and Sporns, 2011). The weighted RC parameter $\Phi^w(k)$ is then computed for each degree k as the total weight $W_{>k}$ normalized over the sum of the weights of the strongest $E_{>k}$ connections of the network (van den Heuvell and Sporns, 2011) which are given by the top $E_{>k}$ ranked weights W_{ranked}. Mathematically, $\Phi^w(k)$ is computed as follows:

$$\Phi^w(k) = \frac{W_k}{\sum_{l=1}^{E_k} w_l^{ranked}} \quad (\mathbf{40})$$

$\Phi^w(k)$ is typically normalized relative to a set of comparable random networks of equal size and degree sequence, resulting in a normalized RC coefficient Φ^w_{norm}(van den Heuvell and Sporns, 2011). In our analysis, 1000 random networks preserving the degree distribution and sequence of the original network (van den Heuvell and Sporns, 2011) were generated, and the RC coefficient was computed for each random network and degree k. $\Phi^w_{random}(k)$ was computed as the average RC coefficient over the random networks and the normalized RC parameter Φ^w_{norm} was computed as

$$\Phi^w_{norm}(k) = \frac{\Phi^w(k)}{\Phi^w_{random}} \quad (\mathbf{41})$$

A network follows an RC organization if $\Phi^w_{norm}(k) > 1$, for a continuous range of k. The randomization process can be used to assess the statistical significance of the results through permutation testing (van den Heuvell and Sporns, 2011). To this respect, the distribution of $\Phi^w_{random}(k)$ yields the null distribution of RC coefficients obtained from random topologies. Using this null distribution, $\Phi^w(k)$ can be assigned a p-value from the percentage of random tests found to be more extreme than the observed RC coefficient $\Phi^w(k)$. All tests were conducted using the Benjamini-Yekutieli procedure (Benjamini and Yekutieli, 2001).

3.4. Attacks on FCGs

SW and RC network organizations have been found to play a central role in overall brain network structure (Xu et al., 2010; Palva and Palva, 2011; van den Heuvell and Sporns, 2011; Dimitriadis et al., 2015) having a strong positive impact on the global efficiency of the network. The RC was proposed by a few studies to better describe structural data (van den Heuvell and Sporns, 2011). To identify the model that describes best the topology of brain connectivity, an "attack strategy" should be adopted (Gallos et al., 2006; van den Heuvell and Sporns, 2011). The attack strategy should focus on SW or RC nodes in order to reveal their importance in the information transfer in the whole network. The role of a node (or a set of nodes) in the level of global efficiency of a network can be evaluated by examining the damage inflicted by attack on that node, simulated as a decrease in the weights of its connections (van den Heuvell and Sporns, 2011).

Two forms of attack were distinguished: "targeted attack" and "random attack to hub connections." In the targeted attack, we randomly selected a set of connections (50 and 100%) that interconnect RC (Target RC – TRC) or SW (Target SW – TSW) nodes and were attacked by two levels, inflicting 50 and 100% damage to all weights of these connections. In the random attack, we restricted the damage to the subset of the connections between RC (Hubs Random RC - HRRC) or SW (Hubs Random SW - HRSW) nodes and the rest of the network. Similar to the target attack, damage was inflicted by reducing the weights of the connections of the selected random set (50 and 100%) by 50 or 100%. To sum up, at each attach strategy, we randomly selected 50 and 100% from each type of connections and then their weights were inflicted by 50 and 100%. Each condition (2 levels of randomly selected subset of connections x 2 levels of damage of weight connections = 4) was applied 1000 times for the RC and SW models.

Finally, we compared the effect of a reduction in global % GE of the network following a targeted attack on SW and RC connections against the effect of a random attack to hub connections. In general, there were more RC than SW nodes in both groups (**Figure 17**). To reduce the bias of the different number of nodes in the two architectures, we selected a subset of RC nodes equal to the number of SW nodes for all four possible attack cases, and to build meaningful statistics we considered 100 different subsets of RC nodes. Finally, we averaged the %GE across all subsets of RC nodes from the 1000 iterations and across the 100 distinct subsets.

Statistical permutation analysis was performed to establish significant GE reductions between the two architectures within and between groups, for each architecture. The threshold for significant p-values was set at 99% level of confidence.

<div align="right">

Chapter 4.

Results

</div>

4.1. Classification performance of Cross Frequency couple

We assessed the classification performance based on the tensorial representation of FCGs with two classifiers, k-NN and ELM, and an ensemble classification scheme (ENS) (**Table 2**). Both the k-NN and ENS showed classification accuracy > 90% in five frequency pairs, while the ELM showed similar performance only in two pairs, δ-β and β-γ_2. The k-NN and ENS approaches also showed high sensitivity, > 90%, with specificity ranging between 85-95%. In contrast, ELM achieved lower sensitivity and specificity values.

Table 2. Summary of classification performance (averaged across 10 – folds of cross-validation) with k-NN, ENS, and ELM classifier.

	Accuracy (%)		
	k-NN	ENS	ELM
δ,β	91.25 ± 13.24	93.33 ± 11.65	90 ± 8.607
δ,γ_1	93.75 ± 6.588	96.67 ± 7.027	76.67 ± 19.56
θ,β	92.5 ± 8.74	90 ±8.607	76.67 ± 21.08
θ,γ_1	93.75 ± 10.62	90 ±11.65	83.33 ± 13.61
β,γ_2	93.75 ± 10.62	96.67 ±7.027	91.67 ± 8.784
	Sensitivity (%)		
δ,β	94 ± 13.5	93.33 ± 21.08	87.5 ± 13.18
δ,γ_1	98 ± 6.325	100 ± 0	82.33 ± 20.95
θ,β	96 ± 8.433	93.33 ± 14.05	75.5 ± 23.52
θ,γ_1	96 ± 12.65	90 ± 22.5	94.17 ± 12.45
β,γ_2	94 ±13.5	96.67 ±10.54	95 ±10.54
	Specificity (%)		
δ,β	86.67 ±23.31	93.33 ±14.05	97.5 ±7.906
δ,γ_1	86.67 ±17.21	93.33 ±14.05	74.33 ±30.7
θ,β	86.67 ±17.21	86.67 ±17.21	87.5 ±22.65
θ,γ_1	90 ±22.5	90 ±16.1	81.17 ±17.12
β,γ_2	93.33 ±14.05	96.67 ±10.54	92.5 ±12.08

4.2. Classification performance and Statistical Differences for Relative Power

Table 3 summarizes the classification performance, the specificity, sensitivity, number of features employed, and their distribution over frequency bands.

Table 3. Classification performance (averaged across 5 – folds of cross-validation) with k-NN classifier.

	k-NN classifier		
	Accuracy (%)	Sensitivity (%)	Specificity (%)
δ and θ	68.14±9.1	65.87 ±5.2	64.75± 10.1

Topographies of group-averaged RP are shown in **Figure 7**, where the white circles denote the significantly different RPs. The main findings are the higher RP for control subjects compared to mTBI in the δ frequency band over bilateral frontal brain areas, while the opposite effect was observed in frequency bands θ to β for mTBI subjects, which demonstrated higher RP over bilateral frontal areas compared to controls.
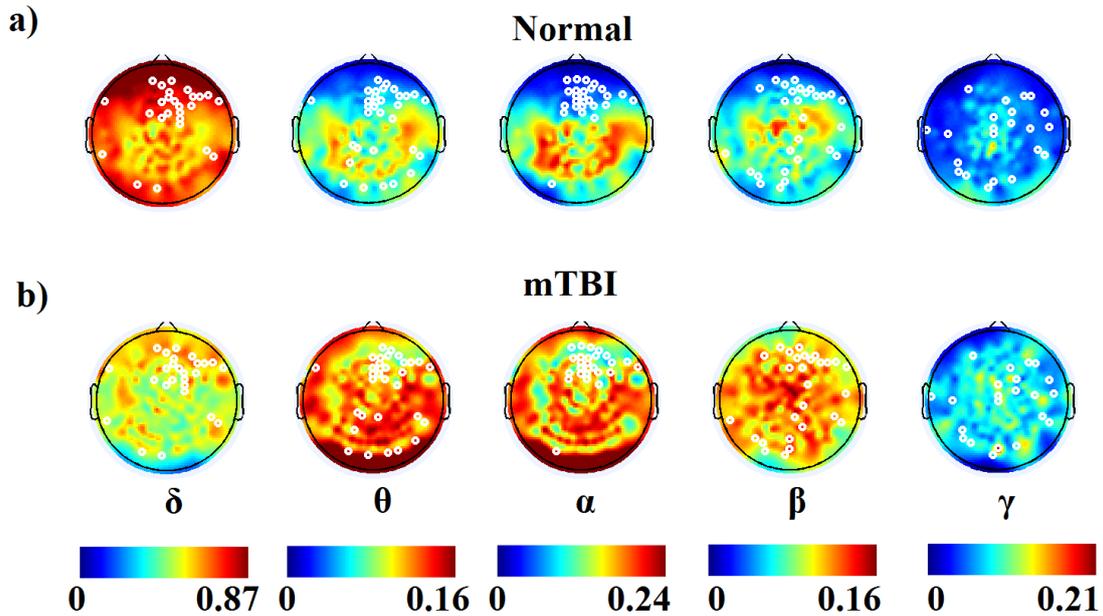
Figure 7. Topography of the mean RP for each frequency band and group. White circles denote the statistically significant group difference of RP at the sensor level, using the Wilcoxon Rank-sum test (p < 0.0001, Bonferroni corrected – p'< p/248).

4.2 Network analysis

Figure 8 and **Figure 9** illustrates the average global and local efficiency, GE and LE respectively, obtained for the two groups. Enlarged circles on the topographical layouts denote statistically significant differences between the two groups (p < 0.05) after adjusting

the p-values for multiple comparisons (Benjamini and Yekutieli, 2001). In particular, based GE topography, the mTBI group shows an enhanced diffuse pattern over anterior-central brain areas bilaterally in δ-β (***Figure 8***.a) and δ-γ1 (***Figure 8***.b), while the control group exhibits an increased activation profile over the entire brain in β-γ2 (***Figure 8***.e). Another interesting topographic difference is the abnormally activated brain area in mTBI located in right frontal regions, involving 9 sensors. This difference is detected on the basis of GE for frequency pairs θ-β (***Figure 8***.c), θ-γ1 (***Figure 8***.d) and β-γ2 (***Figure 8***.e), and on the basis LE for all five frequency pairs (***Figure 9***). Especially for the β-γ2 pair (***Figure 9***.e), all 9 sensors show significantly higher segregation in the mTBI group compared to controls.

Using the measures tabulated by the distance matrix and multi-dimensional scaling (MDS), we projected the 80 individual vectorial LE profiles to distinct points in a reduced 3D space (***Figure 10***.a). We then designed a colored convex hull for each group to visualize the variability and the distance between the two groups in the 3D space. As an estimator of variability within each group, we computed the area of corresponding convex hull. The control group showed a higher variability by a factor of 25 and 40 compared to mTBI for the δ-β and δ-γ$_1$ frequency pairs respectively (***Figure 10***.a).
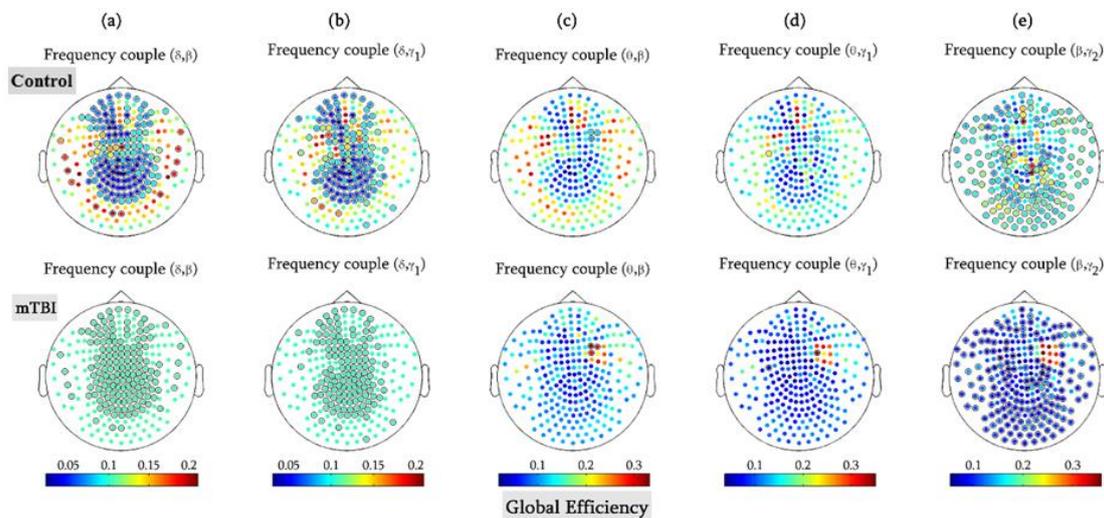
Figure 8. Group-averaged global efficiency (GE) for every sensor in control and mTBI subjects for each pair of frequency bands. Larger circles with a black marker represent statistically significant differences between the two groups (p < 0.05).
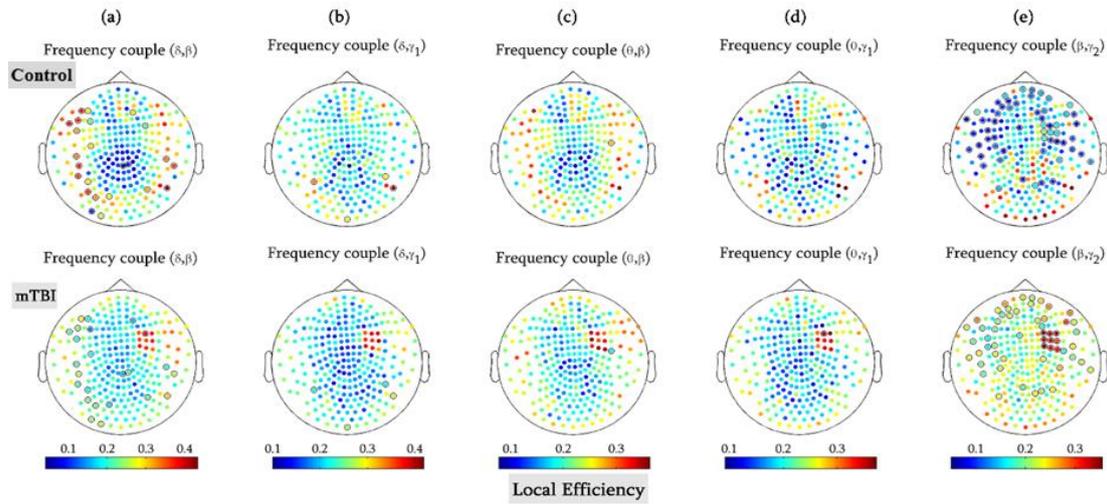
Figure 9. Group-averaged local efficiency (LE) for every sensor in control and mTBI subjects for each pair of frequency bands. Larger circles with a black marker denote statistically significant differences between the two groups (p < 0.05).

Finally, we estimated both GE and LE at the network level and we assessed statistically significant differences using the Wilcoxon rank-sum test and p < 0.001. A significant trend between the two groups was detected only for the β-γ_2 frequency pair, with controls exhibiting higher GE (**Figure 10**.b) and mTBI patients higher LE values (**Figure 10**.b).
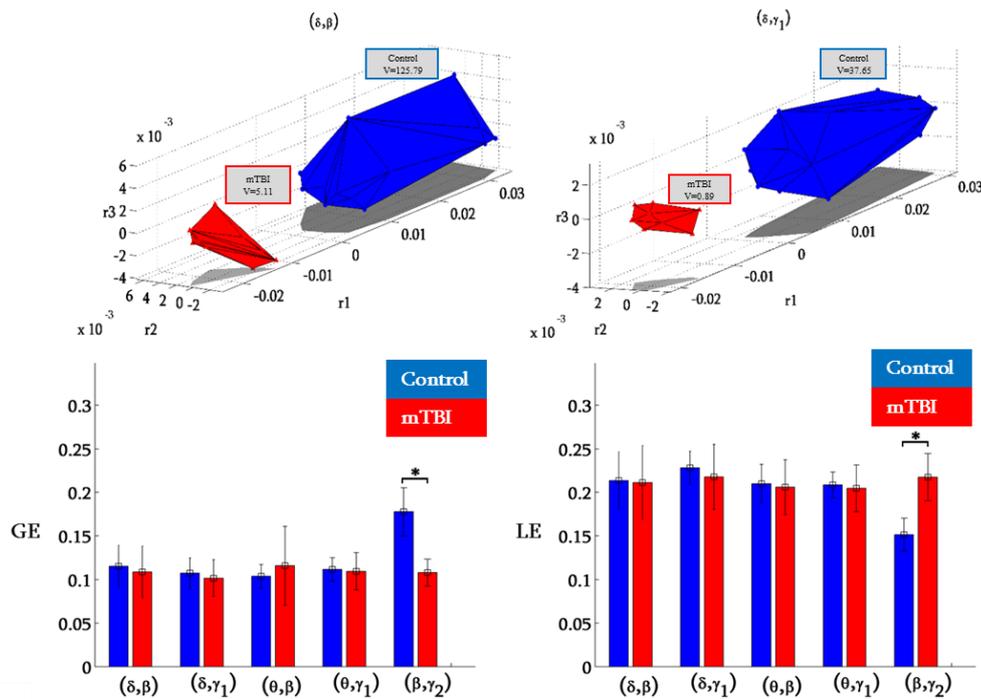
Figure 10. **a)** The illustration of convex hull of the multidimensional scaling reduction to visualize better the total separation of segregated patterns from all subjects for δ-β and δ-γ1, respectively. Label V denotes the area of the convex hull. **b)** Global (GE) and local efficiency (LE) in control and mTBI subjects across the studied frequency pairs (*p < 0.01).

4.3 Community profiles of control and mTBI subjects

Figure 11 illustrates how the variation of information metric, VI, between consecutive iterations of the algorithmic procedure converges to stable a partition, while **Figure 12** presents clustering prototypes for both groups in the five frequency pairs. The five most significant clustering prototypes in the group of controls for the frequency pairs (δ-β), (δ-γ1), and (θ-β) were spatially restricted while in mTBI patients they were more distributed (**Figure 12**.a-c). In frequency pairs (θ-γ1) and (β-γ2), clustering prototypes were spatially scattered in both groups. Furthermore, the organization of functional clusters differed in both groups across the five frequency pairs (**Figure 12****Figure 12**.d, e).
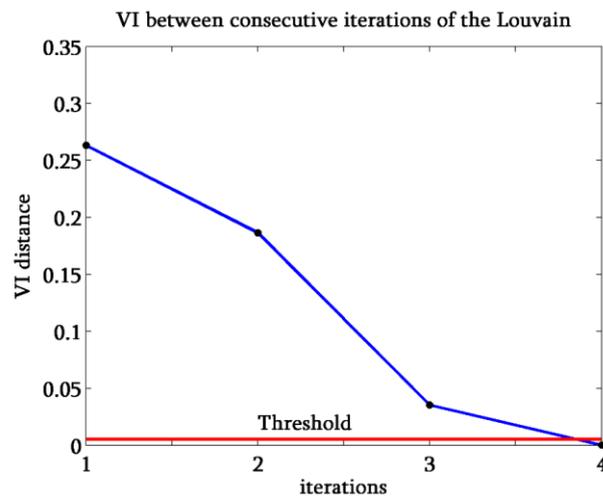
Figure 11. VI values between consecutive iterations of the algorithm used to detect stable clustering prototypes across the two group. The red horizontal line corresponds to a threshold of 0.005 for the difference between the VI iteration t+1 and t.
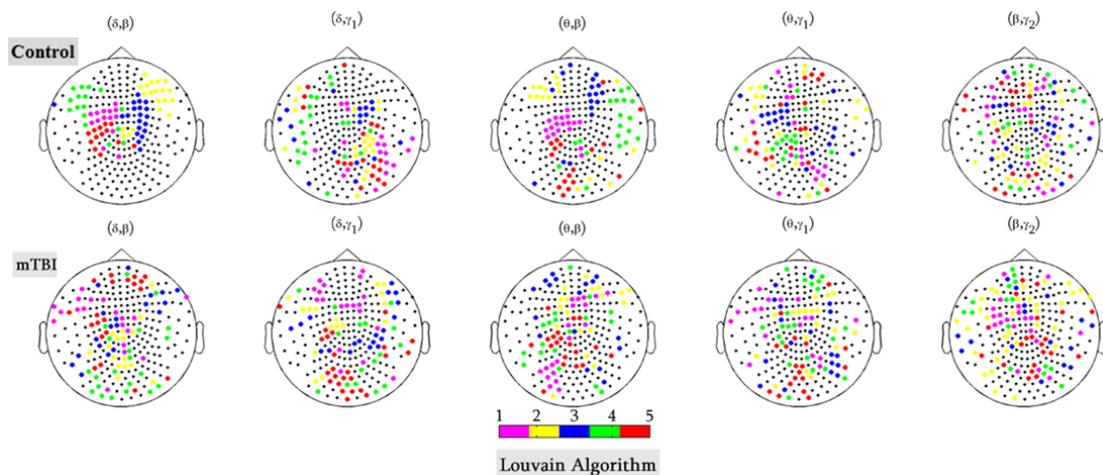
Figure 12. The five prototypical functional segmentations of FCGs with the highest average within-group strength are illustrated for each of the five frequency pairs in the two groups.

4.4 Physical distance of sensors versus PAC strength

To uncover how the strength of CFC was diffused over the Euclidean distance between the sensors in the five frequency pairs across the two groups, we adopted a heat map representation of CFC with physical distance of sensors (**Figure 13**). The adopted illustration (**Figure 13**) gives a clear view of how PAC strength is affected by Euclidean distance in both groups for each CFC-pair. Both Euclidean distance and CFC strength were equally divided into 50 bins. The mean CFC strength was distributed almost equally along the physical distance of sensors in both groups at frequency pairs δ-β (**Figure 13**.a), δ-γ1 (**Figure 13**.b) and θ-β (**Figure 13**.c) but the group of controls showed higher values for the most range of physical distance. For the remaining two frequency pairs, θ-γ$_1$ (**Figure 13**.d) and β-γ$_2$ (**Figure 13**.e), the mean strength in the control group was marginally higher compared to mTBI patients, while mTBI subjects showed a few strong and distant connections on the tail of the distributions.
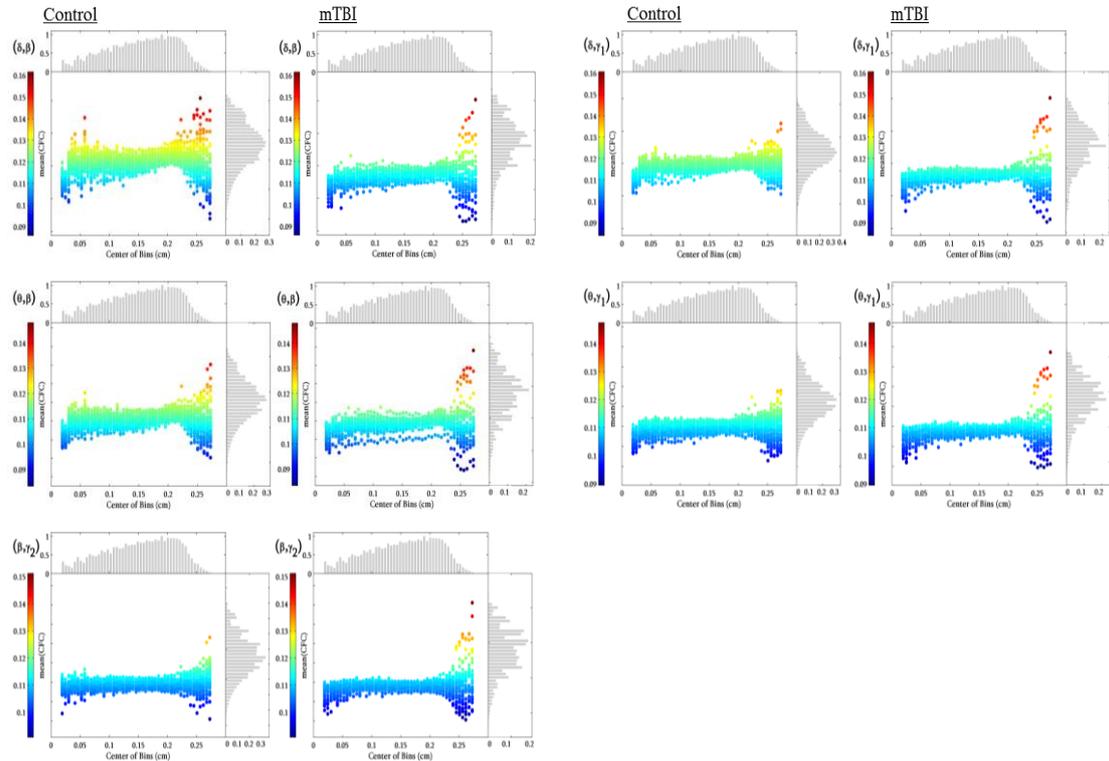
Figure 13. The images illustrate the heat maps (# of subjects x 50 bins). The horizontal image on the top of every heat map presents the histogram of the physical distance among the MEG sensors and the image on the right of the heat maps illustrate the histogram of the connectivity distances.

4.5 CFC Asymmetry and anterior-posterior anisotropy in mTBI

Figure 14 demonstrates for each frequency pair the intra-hemispheric FAI and API indexes in mTBI subjects. The most consistent results among the 30 mTBI subjects are the right lateralization of functional strength in the β-γ_2 frequency pair (**Figure 14**.e; 22 out of 30 subjects) and the anterior predominance of functional strength in δ-β, δ-γ_1, θ-β, and θ-γ_1 frequency pairs in 25, 26, 25, and 24 out of 30 subjects, respectively (**Figure 14**.a-d).
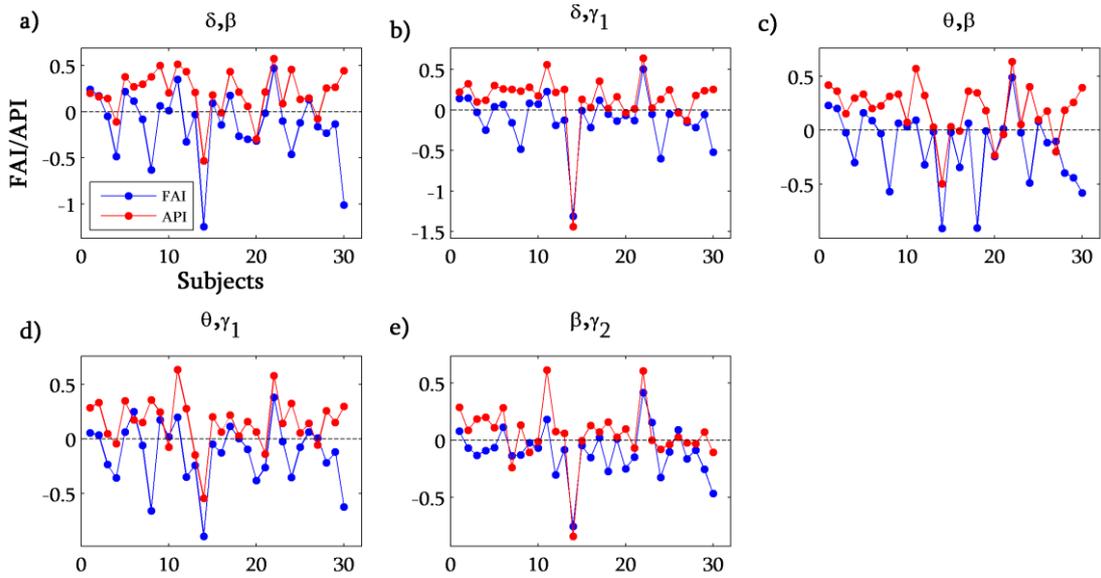
Figure 14. The intra-hemispheric Functional-Coupling Asymmetry (FAI) and anterior-posterior anisotropy (API) in mTBI subjects for each frequency couple.

Table 4 summarizes the distribution of asymmetries of both indexes between the left and right hemispheres and anterior-posterior brain areas in the mTBI group. Finally, functional connectivity strength (FCS) showed a significant trend for higher values in frontal brain regions bilaterally in controls in the δ-β, δ-γ_1, θ-β, and θ-γ_1 frequency pairs (**Figure 15**.a-d) and higher FCS values for the mTBI patients in the β-γ_2 frequency pair (**Figure 15**.e).

Table 4. Number of mTBI subjects showing asymmetric FAI and API values between the left and right hemisphere and between anterior and posterior brain regions.

	δ,β	δ,γ_1	θ,β	θ,γ_1	β,γ_2
FAI (left/right)	11/19	9/21	11/19	12/18	8/22
API (anterior/ posterior)	25/5	26/4	25/5	24/6	18/12
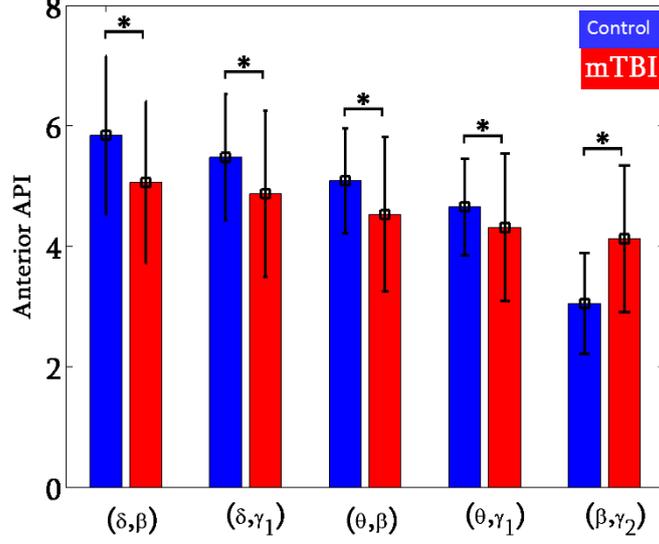
Figure 15. Significant differences of bilateral frontal functional connectivity strength between controls and mTBI patients ($p < 0.01$, Wilcoxon rank-sum test; $p' < p/5$; Bonferroni corrected).

4.6 Results of attack strategies between SW and RC

The tolerance of the SW and RC network organizations are shown in **Figure 16** for both the mTBI and control groups. Each image on **Figure 16** demonstrates which nodes are characterized as SW or RC.

A node of the FCG is characterized as SW node if its S_{ratio} value is higher than the averaged S_{ratio} across all the nodes plus the standard deviation of S_{ratio}. **Figure 16** shows S_{ratio} values for the nodes (i.e. for 248 sensors) and the red dash line demonstrates the corresponding threshold. Note that the mTBI group presented a higher SW threshold (red dashed lines) and fewer SW nodes than the controls (**Figure 16**.a). Finally, the 12% of nodes for control and 6% for mTBI are obtained as nodes of the SW network organization.

The threshold of the RC nodes is demonstrated by the first local maxima which is followed by local minima on the $\Phi_{norm}(k)$ curve (**Figure 16**.b: red point). Therefore, RC nodes are those nodes that are equal or higher than the red point local maxima. In addition, verifying the RC organization indicated by a significant tendency of highly connected nodes; the RC nodes demonstrated with a red dot (**Figure 16**.b) for both groups. In particular, it is derived that up to 55% of nodes for control and 40% for mTBI demonstrate more connectivity than expected by chance ($p < 0.05$, BY procedure; Benjamini and Yekutieli, 2001, **Figure 16**.b). Finally, control group has higher degree (k=118) than the mTBI group (k=98).
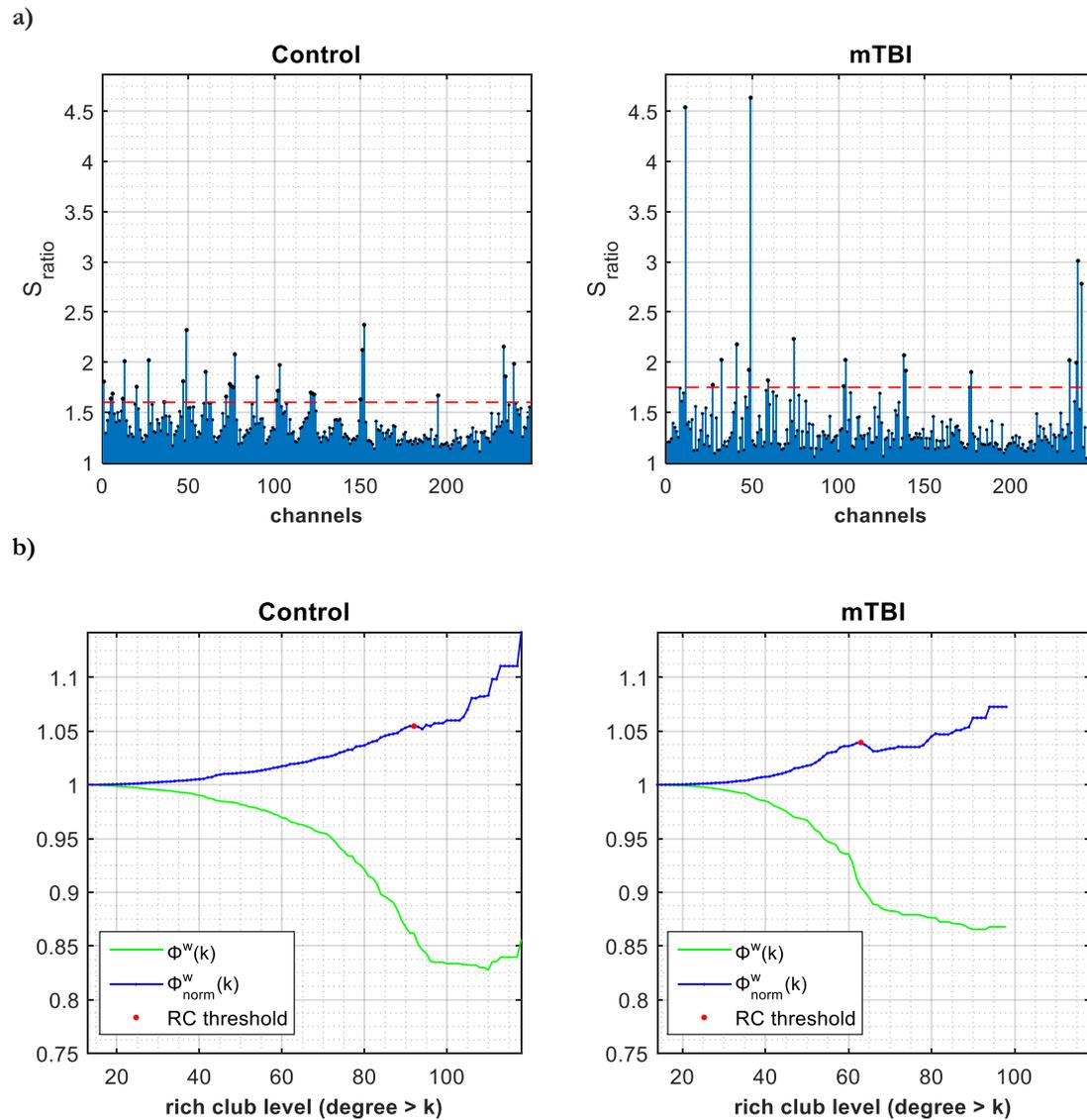
Figure 16. Comparison of mTBI subjects against controls for the (δ,β) frequency couple. **a)** SW curves: SW nodes (black points) and SW threshold (red dashed line) for each group. **b)** RC curve with significant (red points) and non-significant (blue points) degrees. The red point demonstrates the lowest degree of the RC nodes.

Various topological arrangements for each network organization (SW or RC) and mean strength of every node for each group are illustrated in **Figure 17**. In general the nodal strength is the sum of weights of links connected to the node. The nodal in-strength is the sum of inward link weights and the nodal out-strength is the sum of outward link weights.

In the control group, the SW nodes are located primarily in frontal and central brain areas and in the mTBI the SW nodes are located to central-parietal regions (**Figure 17**.a). All results are about the averaged FCG across control and mTBI groups separately for the (δ, β) frequency couple. The RC nodes in control group are found in prefrontal, temporal, and occipital region bilaterally and a similar pattern is observed in mTBI subjects but with

fewer nodes and more scattered compared to controls (***Figure 17***.b). It seems that the RC network organization represent nodes with high out-strength while SW network organization includes nodes with low out-strength (***Figure 17***.c). ***Figure 17*** confirms the theory that RC have disproportionately dense interconnections and high number of shortest paths and the SW organization includes nodes which can communicate with any other node over a few 'hops' (i.e. first degree). In particular, nodes with high nodal out-strength (for example, nodes in the left and right temporal side: ***Figure 17***.c, topography on the right corner) are presented as RC nodes with high number of connections (***Figure 17***.c, topography on the middle right side – red edges). However, nodes with low nodal out-strength (for example, nodes in the central side: ***Figure 17***.c, topography on the right corner) presents a SW behavior (***Figure 17***.c, topography in the middle right side – blue edges). Finally, there are nodes that can be simultaneously part of RC and SW organization as it is presented by ***Figure 17***.d.
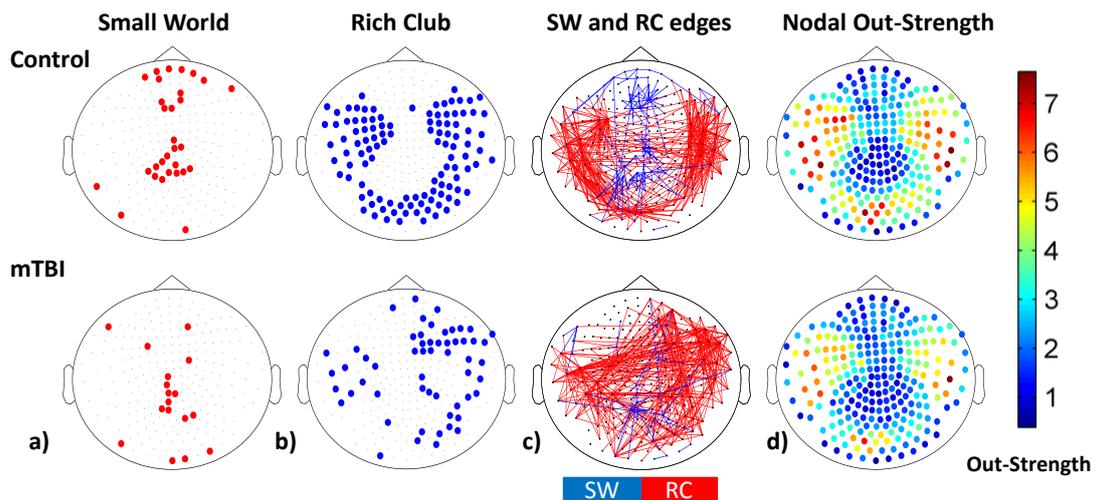
Figure 17. Topographies of **a)** SW topology (red dots), **b)** RC topology (black dots), **c)** the RC and SW network organizations; Blue nodes (edges) present the SW network organization and the red nodes (edges) show the RC network organization **d)** nodal out-strength.

The results from the attack strategy of the RC and SW organization can be used to estimate the reduction in network GE, as demonstrated in ***Figure 18***. The attack strategy adopts two type of simulation, an attack (i.e. edge weight reduction) among the SW or RC nodes (T) and an attack among the SW or RC nodes to the rest of nodes (Hubs Random – HR). For each case (T or HR) two scenarios simulate the attack, 50% and 100% of edge weight reduction only for the 50% of weight edges of the brain network.
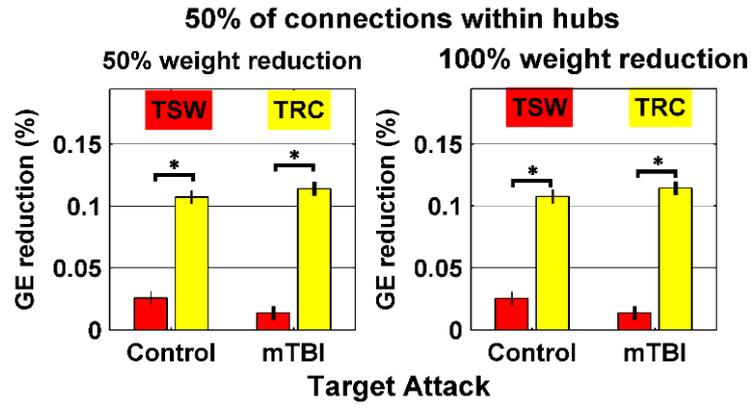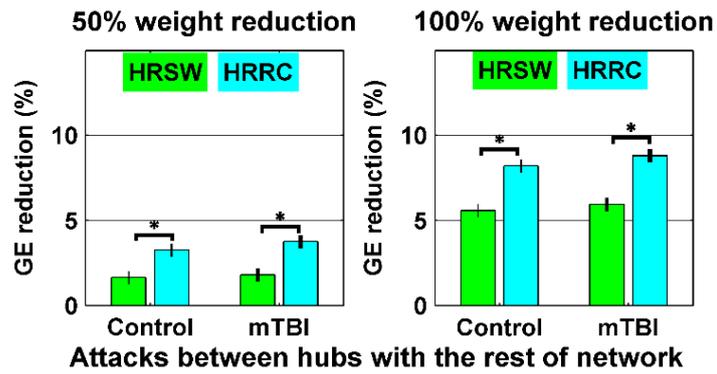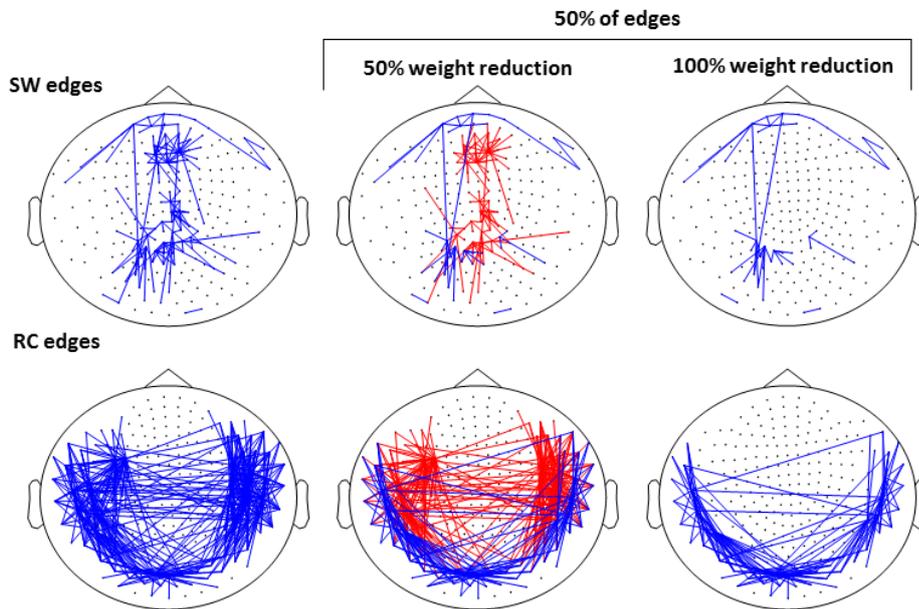
Figure 18. Reduction in total GE as a result of **a)** TSW-red and TRC-yellow bars and **b)** HRSW-green and HRRC-cyan bars. All comparisons (paired test linked by *) reach statistical significance (p-value < 0.0001). **c)** A graphical representation of the attack strategy in case of nodes to the rest of brain network.

To reduce the bias of the different number of nodes in the two architectures, a subset of RC nodes equal to the number of SW nodes for all four possible attack cases.

The percentage of the total GE reduction is significantly higher for the RC model (TRC – yellow bars and HRRC – cyan bars) than the SW (TSW – red bars and HRRC – green bars) model for both groups on each level of weight reduction on interconnected nodes (50% or 100%) (**Figure 18**. a-b). The brain networks on the left of figure demonstrate the SW (left top) and RC (left bottom) edges (blue edges) before the attack simulation. The middle brain networks show the 50% weight reduction (red edges) and the right images shows the edges after 100% weight reduction. Both attacks are for the 50% of total edges for the corresponding brain networks. Current figure present only the outward link weights for the control group. All the topographies have same edges for each network organization. In particular, the reduction in total GE caused by random attacks in both architectures is higher for the mTBI group compared to the control group (p-value < 0.001). Furthermore, the GE reduction is more pronounced when a targeted attack to connections within nodes affects the RC organization compared to SW organization, but at a lower percent level (<1%) from a random attack. Moreover, comparing GE reduction between the two levels of weight reduction (50% and 100%) for target attack, the difference between them is extremely small (.a) due to the small number of edges among nodes of each of the models (SW or RC). However, higher GE reduction is revealed by the 100% weight reduction than 50% of weight reduction in case of attack among RC or SW nodes the rest of nodes (**Figure 18**.b). This evidence is strongly supported by .c which presents the edges (blue edges) of each organization before each level of weight reduction for the attack of hubs to the rest of nodes (left topographies) for control group. In particular, the middle topographies of **Figure 18**.c present the 50% of total outward weight edges for both of organizations is attacked (i.e. 50% weight reduction – red edges). Furthermore, the right topographies present only those edges that they are not affected by the attack (i.e. 100% weight reduction) while the other edges are disappeared. It is important to note that the attack strategy is performed on random subsets of SW and RC nodes. However, same number of edges is presented by **Figure 18**.c for both of weight reductions (i.e. 50% and 100%). All comparisons presented show statistical significance, so overall, the percentage of GE reduction is significantly different across the two architectures (SW vs RC). Therefore, the averaged FCGs for the frequency couple (δ,β) follow a rich-club organization due to its higher GE reduction.

4.7 Utilization of networks approaches

In the current study, network metrics and approaches are used in order to prove that CFC relation consists a promising and suitable biomarker about resting state MEG of mTBIs. Indeed, the CFC metric is revealed as a suitable biomarker according to the above results. In particular, the discrimination of CFC relations between mTBI and control was high (>90%). Furthermore, a clear separation on the convex hull of the LE is revealed between two groups. Moreover, significant differences are also estimated on the LE and GE of the CFC FCGs. Overall CFC relation on the resting state MEG can easy diagnose the mTBI.

The thresholded scheme does not include a network tool in order to reduce the total number of edges, (i.e. the use of the cost function, GCE) only for brain networks. The current thresholded scheme can easily be used in other type of networks like social, internet electric power etc. due to simple linear form which includes the GE. For example, in case of a social network is often hard to manage greatly high number of edges. However, it is easy to estimate the GE and remaining only the significant edges according to the criterion of the GCE.

The above results identified that RC organization describes better the topology of brain connectivity for the resting MEG FCGs. The RC organization includes lower number of nodes than the initial brain network and as a result fewer edges (***Figure 17***). This property directly results in the usage of the RC organization and not the usage of the initial thresholded brain network for the investigation of a disease such as mTBI. The advantage of the usage the RC organization is that fewer nodes (i.e. hubs – highly connected nodes) are used significantly and as a result the most important properties of the initial network are still maintained. Therefore, it would be to perform estimation of the above network approaches such as the estimation of the convex hull for the visualization of the variability and the distance between two groups in the 3D space or the calculation of the physical distances to uncover how the strength of CFC was diffused over the Euclidean distance between sensors. The current described scenario can easily be used by different type network such as internet or social. Finally, the current attack strategy is not eliminated by using only on brain networks due to its usage in other study of different network type (diffusion tensor imaging - van den Heuvell and Sporns, 2011; scale-free networks - Gallos et al., 2006; social networks - Albert and Barabasi, 2002).

Chapter 5.
Discussion

In this study, we analyzed resting state brain networks using MEG recordings obtained from 50 controls and 30 mTBI patients, under the notion of phase-amplitude coupling. Our main goal was to investigate how cross-frequency coupling on MEG spontaneous activity is affected in mTBI patients compared to control subjects. PAC estimates show that oscillatory activity of higher frequencies is modulated by the phase of slower spontaneous frequencies. We estimated PAC between sensors in a pair-wise fashion and among every possible pair of frequency bands using the concept of MI. In addition, using a tensor representation of the CFC directed graphs and tensor subspace analysis for optimal feature extraction, we showed that mTBI patients could be separated from controls with more than 90% classification accuracy for the frequency couples (δ, β), (δ, γ1), (θ, β), (θ,γ1) and (β,γ2) (***Table 2***). Classification performance based on relative power at the sensor level succeeded to discriminate mTBI from control subjects with only a 70% accuracy (***Table 3***). A prominent asymmetry between hemispheres in the interdependencies among mTBI subjects was observed with a right lateralization of FAI in the β-γ2 frequency pair. The dominant API was observed with anterior predominance in most of frequency pair. Additionally, estimation of FCS within bilateral frontal brain areas revealed significantly higher values for controls compared to mTBI subjects in most of frequency pairs, while significantly higher FCS values were observed for mTBI patients compared to controls in the β-γ2 frequency pair.

The classification scheme that included the feature extraction algorithm of Laplacian scores revealed significant differences in RP in the δ and θ frequency band mainly in frontal brain areas (***Figure 7***). The findings related to the δ frequency band could be attributed possibly to the deactivation of the default mode network (DMN) resulting from inhibitory mechanisms activated during mental tasks (Dimitriadis et al., 2010). This finding may also reflect a less 'standby' DMN network for mTBI that otherwise would be ready to be activated during a cognitive task. The higher RPs for mTBI subjects in the θ frequency band over frontal areas could be interpreted as a compensatory mechanism to lower RP in the δ band for keeping the reflexibility of the cognitive state during spontaneous activity on a 'quasi-normal' level (Scheeringa et al., 2008).

A recent study (Dimitriadis et al., 2015) analyzed the same dataset under the perspective of FCGs computed by quantifying the functional connectivity between sensors with the phase-locking value (PLV). That analysis also examined the notion of intra-frequency coupling and provided initial evidence of how it is affected by mTBI by employing MEG at resting-state (Dimitriadis et al., 2015). In the present study we explored how CFC via PAC estimation is affected in mTBI at resting-state, in an attempt to illustrate a communication mechanism among frequency bands, in addition to the mere phase synchronization. By employing a PAC estimator for quantifying CFC brain networks and adopting a tensorial treatment for the classification procedure, we derived biomarkers that could prove valuable for the evaluation of mTBI.

Further complex network analysis of PAC brain networks revealed significant differences between the two groups. By the contrast of nodal GE and LE (*Figure 8* and *Figure 9*) between the two groups, an abnormally activated brain area was revealed in mTBI subjects, located over the right frontal area, that showed high levels of integration and segregation, as quantified by GE and LE, respectively (*Figure 8*.c, d, e and *Figure 9*.a-e). The control group also showed a dense network of stronger local and global connections compared to mTBI in the five frequency pairs (*Figure 10*.a).

The structure of the five most significant functional clusters in both groups across the five frequency pairs differed significantly (*Figure 12*). Specifically, for frequency pairs (δ-β), (δ-γ1), and (θ-β) (*Figure 12*.a-c), the five most significant clusters were spatially restricted in control groups compared to a more dispersed distribution in the mTBI group. Both groups demonstrated spatially scattered functional clusters in the frequency pairs (θ-γ1) and (β-γ2), but with different functional organization (*Figure 12*.d, e). Finally, the mean strength in controls was marginally higher compared to mTBI subjects, while mTBI showed a few strong and distant connections in the tail of the distributions (*Figure 13*.d and *Figure 13*.e). Overall, our findings suggest a higher functional integration for the controls compared to mTBI subjects.

It has already been demonstrated that the CFC and (particularly) the PAC play an important role in the communication between regions that produce different brain rhythms (Palva et al., 2005; Canolty et al, 2010), especially as principle mechanism of how local oscillatory activity of low frequency is interacting with distant brain areas functioning at higher frequency (Florin et al., 2015). Results of recent studies in both animals and humans support a mechanism that oscillations at higher frequencies are often modulated

by the phase of slower phase fluctuations (Osipova et al., 2008; Tort et al., 2008, 2009, 2010; Cohen et al., 2009a, b; Colgin et al., 2009; Axmacher et al., 2010a, b; Voytek et al., 2010). Important elements of nonlinear coupling across different frequencies reveal different types of CFC, such as phase-amplitude coupling (Tort et al., 2008, 2009, 2010; Cohen et al., 2009a,b; Colgin et al., 2009; Axmacher et al., 2010a,b), n:m phase locking (Dimitriadis et al., 2014), or amplitude-amplitude coupling (Hipp et al., 2012; Engel et al., 2013). Cross-frequency coupling of the spontaneous activity is altered during development (Pinal et al., 2015) and brain disorders/diseases due to structural and/or functional network alterations (Engel et al., 2013).

Only a few MEG studies explore CFC interactions at both resting-state and active tasks in normal and diseased populations. Recently, Florin et al. (2015) using resting state MEG demonstrated that phase-amplitude coupling provides a mechanism for brain network formation, which reconciles previous findings and theories on long-range communication between neural populations. It confirms and extends previous findings in healthy participants of PAC as a key mechanism that support long-range brain synchronization (Palva et al., 2005; Canolty et al., 2006; Osipova, Hermes, and Jensen, 2008).

Topologically, our study revealed significant trends regarding the functional strength of CFC interactions. The anterior predominance of functional connectivity strength (FCS) (API) in δ-β, δ-γ1, θ-β, and θ-γ1 frequency pairs is observed in the majority of mTBI subjects, specifically in 25, 26, 25, and 24 out of 30 subjects, respectively (***Figure 14***.a-d). Moreover, consistent results among the 30 mTBI subjects are obtained for the right lateralization of functional strength in β-γ2 frequency couple (***Figure 14***.e; 22 out of 30 subjects). Finally, FCS within bilateral frontal brain regions showed significant higher values for control over mTBI subjects in δ-β, δ-γ1, θ-β and θ-γ1 (***Figure 14***.a-d) and a higher FCS for mTBI over control subjects in β-γ2 (***Figure 14***.e). Our findings demonstrate that frontal brain areas are more vulnerable to brain injury and this is reflected by the lower FCS observed in mTBI subjects compared to controls in four frequency pairs (***Figure 14***) (Eierud et al., 2014). These findings based on the δ band being the modulating frequency could reflect a lower deactivation of default mode network for mTBI subjects and could be attributed to inhibitory mechanisms activated at resting-state (Dimitriadis et al., 2010b). Findings based on the θ band being the modulating frequency could be related with a lower activated level of working memory at rest for mTBI, which can be interpreted as a lower reflex stand-by level ready to be activated during a cognitive task (D'Esposito

et al., 1995). The role of activity in the β frequency is less studied and understood. A recent review suggested that activity in the β frequency band might be associated with the maintenance of motor sets and cognition (Engel and Fries, 2010). The significant higher FCS for mTBI compared to controls in β-γ2 may be associated with a balanced mechanism of the brain to keep the cognition on a quasi-normal level.

The current study adopted an attack strategy on RC and SW nodes to estimate the damage to GE of functional connectivity networks computed from resting state MEG. We hypothesized that the highest reduction in global efficiency (GE) caused by a targeted attack on each network organization's nodes would reveal the organization that better describes the underlying brain networks. GE is an indicator of global information integration through the network and its highest drop-off stage can derive a reliable estimator of the significant group of hubs as the functional core of the brain network.

We found that the RC organization undergoes significantly higher damage in GE than the SW organization for both groups and that this reduction is higher in the mTBI group. According to the above results (**Figure 18**.a-b), it seems that reduction in total GE after random attack was more pronounced in RC organization compared to the SW organization in both groups. Based on our hypothesis, these findings would suggest that resting state MEG connectivity networks follow a rich-club organization. There is clear evidence that resting-state activity is shaped by cross-frequency phase-to-amplitude coupling (PAC) (Floring and Baillet, 2014). A recent study (Schroeter et al., 2015) also suggest that RC organization served as broker of spontaneous activity flow, confirming that hub nodes and rich-clubs may play an important role in coordinating functional dynamics at the microcircuit level. In the present study, we showed that the RC topology captures more efficiently the effects of mTBI in the PAC brain- networks at the resting state.

5.1. Conclusion

In summary, this study first demonstrated that the orchestration of brain resting-state networks is inefficient in mTBI subjects and the key mechanism of this collapse is CFC. Moreover, the treatment of cross-frequency FCGs as tensors on five frequency pairs succeeded to separate correctly mTBI from controls, with higher than 90% classification accuracy. Therefore, MEG-CFC brain networks computed with PAC at rest with a tensorial representation could form a valuable connectomic biomarker for the diagnosis of

mTBI. In addition, further complex network analysis of PAC brain networks revealed significant differences between the two groups. An abnormally activated brain area was revealed in mTBI subjects, located over the right frontal area that showed high levels of integration and segregation, as quantified by GE and LE, respectively. The control group also showed a dense network of stronger local and global connections compared to mTBI in the five frequency pairs. Furthermore, the structure of the five most significant functional clusters in both groups across the five frequency pairs differed significantly suggests a higher functional integration for the controls compared to mTBI subjects. Significant trends are also revealed by the functional strength of CFC interactions. The anterior predominance of functional connectivity strength (FCS) is observed in the majority of mTBI subjects. Another evidence was that the frontal brain areas are more vulnerable to brain injury and this is reflected by the lower FCS observed in mTBI subjects compared to controls in four frequency pairs. Our study confirms and extends previous findings in healthy participants of PAC as a key mechanism that support long-range brain synchronization that only a few MEG studies explore CFC interactions at both resting-state and active tasks in normal and diseased populations. Finally, there is clear evidence that resting-state activity is shaped by cross-frequency phase-to-amplitude coupling (PAC) (Floring and Baillet, 2014) and in the present study, we showed that the RC topology captures more efficiently the effects of mTBI in the PAC brain- networks at the resting state. Moreover, results suggest that resting state MEG connectivity networks follow a rich-club organization.

Overall, current study suggests that the combination of the CFC couples, network metrics and the RC network organization reveals on MEG resting state recordings can be stand as an appropriate and efficient connectomic biomarker for mTBIs' diagnosis and for different type of networks (real-life networks) due to the utilization of the current scheme of network approaches that current study successful combined.

5.2. Future Work

A deep investigation of the classification parameters in order to improve the classification scores. Greedy search approaches will improve the research in for the revelation of the optimal parameters. Probably, the examination of possible classification scenarios using boosting techniques and random forests in order to reveal better discrimination (i.e. >95%).

The comparison between small world and rich club organization were performed only for a specific frequency couple and for CFC metric. It would be interesting to estimate and show whenever the resting state MEG connectivity networks better fit the rich-club organization for most of the frequency couples and not only for CFC couples but also for interdependent synchronization coupling like mutual information.

To provide a robust mapping of how the brain functions at the resting-state and during cognition in both healthy and disease subjects, it is necessary to adopt a dynamic functional connectivity approach (Dimitriadis et al., 2010a, 2012a, b, c, 2013a, b, 2014, 2015) through the definition of Functional Connectivity Microstates, FC-μstates (Dimitriadis et al., 2013a) and/or network microstates, Net-μstates (Dimitriadis et al., 2015). Moreover, In particular, the symbolic dynamical signatures will be mapped the time-varying functional connectivity graphs (TVFCGs) to multivariate nodal network metrics time series (nNMTS) of global/local efficiency estimates, performing an elaborate study over CFC segregation dynamics and then characterizing TVFCGs with a small number of stable states that can be called 'CFC-network-level microstates (nμstatesCFC). Furthermore, the automated inference of Quantized Stochastic Processes (QSP): stochastic dynamical systems that evolve over discrete time, and yield sample paths, which are sequences over a pre-specified symbolic alphabet. Under the assumptions of stationarity and ergodicity, any such quantized process may be generated by a probabilistic automata. A probabilistic automata, syntactically, is a directed graph whose edges are labeled with alphabet symbols, and the associated transition probabilities. A probabilistic automata with a finite number of nodes (in its minimal description) is a Probabilistic Finite State Automata (PFSA) (Chattopadhyay and Lipson, 1984). Finally, our future studies with mTBI subjects will focus on dynamic cross-frequency coupling, their related FC-μstates, and their symbolic dynamical signature on MEG resting-state. As a results, the dynamic estimation of the Small World and Rich Club organization and how the groups (i.e. Control and mTBI) differ on time-variations. Using a dynamic attack strategy, it would be better to estimate the type of brain network in time and using a static way like the current study.

Appendix A

Subject demographics for the current mTBI group.

Subject	Age at injury	Gender	Auto Pedestrian - frontal	Auto Pedestrian - frontal Type	Auto Pedestrian - frontal _Location
1	21.7	M	Auto Pedestrian	Laceration - no sutures	Head
2	42.0	M	Motor Vehicle	Abrasion	Head
3	22.1	M	Motor Vehicle	Tenderness	Head
4	43.1	M	Motor Vehicle	Tenderness	Head
5	34.6	M	Fall Raised Surface	Abrasion	Head
6	42.3	F	Assault	Bruising	Head
7	20.3	M	Motor Vehicle	Bruising	Head
8	24.0	F	ATV	Laceration - no sutures	Head
9	24.9	M	Sports-related	Laceration - with sutures	Head
10	24.4	F	Motor Vehicle	Bruising	Head/Face
11	43.7	F	Motor Vehicle	Tenderness	Head
12	36.3	M	Blow to Head	Tenderness	Head
13	49.1	M	Motorcycle	Contusion	Head
14	43.3	F	Fall Standing	Laceration - no sutures	Head
15	23.3	F	Fall Standing	Laceration - with sutures	Head
16	33.4	M	Fall Raised Surface	Laceration - no sutures	Head
17	27.3	M	Auto Pedestrian	Tenderness	Head/Face
18	49.8	F	Fall Moving Object	Laceration - with sutures	Head
19	25.3	M	Fall	Abrasion	Head
20	27.7	M	Fall Moving Object	Abrasion	Head
21	20.5	M	Motor Vehicle	Bruising	Head
22	27.0	F	Auto Pedestrian	Bruising	Head
23	22.6	F	Motor Vehicle	Contusion	Head
24	34.8	M	Assault	Contusion	Head
25	20.3	M	Sports-related	Contusion	Head/Face
26	43.8	F	Fall Standing	Contusion	Head
27	28.8	F	Motor Vehicle	Contusion	Head
28	27.8	M	Assault	Contusion	Head
29	24.7	F	Assault	Contusion	Head
30	22.8	F			

References

Achard, S., Bullmore, E., 2007. Efficiency and cost of economical brain functional networks. PLoS Comput Biol 3, e17.

Aertsen, A., Gerstein, G.L., Habib, M.K., Palm, G., 1989. Dynamics of neuronal firing correlation: modulation of effective connectivity. J of Neurophysiology 61, 900–917.

Albert, R. Barabási A.-L., (2002). Statistical mechanics of complex networks. Reviews of Modern Physics 74, 47-97.

Antonakakis, M., Giannakakis, G., Tsiknakis, M., Micheloyannis, S. and Zervakis, M., 2013. Synchronization coupling investigation using ICA cluster analysis in resting MEG signals in Reading Difficulties. Bioinfo and Bioeng (BIBE), 2013 IEEE 13th International Conference on, 1-5.

Axmacher, N., Cohen, M.X., Fell, J., Haupt, S., Dümpelmann, M., Elger, C.E., 2010a. Intracranial EEG correlates of expectancy and memory formation in the human hippocampus and nucleusaccum- bens. Neuron 65, 541–549.

Axmacher, N., Henseler, M.M., Jensen, O., Weinreich, I., Elger, C.E., and Fell, J., 2010b. Cross-frequency coupling supports multiitem working memory in the human hippocampus. *Proc.Natl.Acad. Sci.U.S.A.* 107, 3228–3233.

Bassett, D.S., Bullmore, E.T., Meyer-Lindenberg, A., Apud, J.A., Weinberger, D.R., Coppola, R., 2009. Cognitive fitness of cost-efficient brain functional networks. Proc. Natl. Acad. Sci. USA 106, 11747–11752.

Bassett, D.S., Meyer-Lindenberg, A., Achard, S., Duke, T., Bullmore, E.T., 2006. Adaptive reconfiguration of fractal small-world human brain functional networks. Proc Natl Acad Sci USA 103, 19518–19523.

Bertoni, A., Folgieri, R., Valentini, G., 2005. Bio-molecular cancer prediction with random subspace ensembles of support vector machines, Neurocomputing 63, 535– 539.

Bigler, E.D., 2013. Neuroimaging Biomarkers in Mild Traumatic Brain Injury (mTBI. Neuropsychol Rev (2013) 23:169–209.

Bigler, E.D., Orrison, W.W., 2004. Neuroimaging in sports-related brain injury. In: Lovell, M. R., Echemendia, R.J., Barth, J.T., Collins, M.W. (Eds.), Traumatic Brain Injury in Sports: An International Perspective. Lisse, Netherlands, Swets and Zeitlinger, 71–94.

Blondel, VD, Guillaume, J-L, Lambiotte, R, Lefebvre, E, (2008). Fast unfolding of communities in large networks, J Statistical Mechanics: Theory and Experiment 2008(10), P10008 (12pp).

Boccaletti, S., Latora, V., Moreno, Y., Chavez, M., Hwang, D.U., 2006. Complex networks: Structure and dynamics. Phys Rep 424, 175-308.

Bruns, A. and Eckhorn, R., 2004. Task-related coupling from high-to low-frequency signals among visual cortical areas in human subdural recordings. Int. J. Psychophysiol. 51, 97–116.

Bullmore, E., and Sporns, O. 2012. The economy of brain network organization. Nature Reviews Neuroscience 13:336–349.

Bullmore, E., Sporns O., 2009. Complex brain networks: graph theoretical analysis of structural and functional systems. Nature Reviews Neuroscience 10, 186-198.

Canolty, R.T. and Knight, R.T, 2010. The functional role of cross-frequency coupling, Trends Cogn. Sci. 14(11), 506-15.

Canolty, R.T. et al. 2006. High gamma power is phase-locked to theta oscillations in human neocortex. Science 313, 1626–1628.

Carr J., and Brown J., 2001. Introduction to biomedical equipment technology. Prentice-Hall, New Jersey, USA, 4th edition.S

Cassidy, J.D., Carroll, L.J., Peloso, P.M., Borg, J., von Holst, H., Holm, L., 2004. WHO Collaborating Centre Task Force on Mild Traumatic Brain, Injury, Incidence, risk factors and prevention of mild traumatic brain injury: results of the WHO Collaborating Centre Task Force on Mild Traumatic Brain Injury. J Rehabil Med 36(43), 28-60.

Castellanos, N.P., Paul, N., Ordoñez, V.E., Demuynck, O., Bajo, R., Campo, P., Bilbao, A., Ortiz, del Pozo, F., Maestú, F., 2010. Reorganization of functional connectivity as a correlate of cognitive recovery in acquired brain injury. Brain 133, 2365–2381.

Chattopadhyay I. and Lipson, H., 1984. "Abductive learning of quantized stochastic processes with probabilistic finite automata", Philosophical Transactions of The Royal Society A, 371, 20110543.

Cichocki, A., R. Zdunek, A. H. Phan, and S. Amari. Nonnegative Matrix and Tensor Factorizations: Applications to Exploratory Multi-Way Data Analysis and Blind Source Separation. Chichester: Wiley, 2009.

Cohen, M.X. 2008. Assessing transient cross-frequency coupling in EEG data. J. Neurosci. Methods 168, 494–499.

Cohen, M.X., Axmacher, N., Lenartz, D., Elger, C.E., Sturm, V. and Schlaepfer, T.E., 2009a. Good vibrations: cross-frequency coupling in the human nucleus accumbens during reward processing. *J. Cogn. Neurosci.* 21, 875–889.

Cohen, M.X., Elger, C.E., and Fell, J., 2009b. Oscillatory activity and phase-amplitude coupling in the human medial frontal cortex during decision making. *J. Cogn. Neurosci.* 21, 390–402.

Colgin, L.L., Denninger, T., Fyhn, M., Hafting, T., Bonnevie, T., Jensen, O., 2009. Frequency of gamma oscillations routes flow of information in the hippocampus. *Nature* 462, 353–357.

Conover, W.J., 1980. Practical Nonparametric Statistics. Hoboken, NJ: John Wiley & Sons, Inc.

Contreras, D., and Steriade, M., 1997. Synchronization of low-frequency rhythms in corticothalamic networks. Neuroscience 76, 11–24.

D'Esposito, M., Detre, J.A., Alsop, D.C., Shin, R.K., Atlas, S., 1995. The neural basis of the central executive system of working memory. Nature 378, 279–281.

De Monte, V.E., Geffen, G.M., Massavelli, B.M., 2006. The effects of post-traumatic amnesia on information processing following mild traumatic brain injury. Brain Inj. 20, 1345–1354.

Delorme, A., Makeig, S., 2004. EEGLAB: an open source toolbox for analysis of single-trial EEG dynamics including independent component analysis. J. Neurosci. Methods 134, 9-21.

Destexhe, A., Contreras, D., and Steriade, M., 1999. Spatiotemporal analysis of local field potentials and unit discharges in cat cerebral cortex during natural wake and sleep states. J. Neurosci. 19, 4595–4608.

Dietterich, T.G. Ensemble methods in machine learning. In: Proceedings of Multiple Classifier.

Dimitriadis, S. I., Y. Sun, K. Kwok, N. A. Laskaris, and A. Bezerianos. A tensorial approach to access cognitive workload related to mental arithmetic from eeg functional connectivity estimates. Conf. Proc. IEEE Eng. Med. Biol. Soc. 2013:2940–2943, 2013.

Dimitriadis, S.I., Kanatsouli, K., Laskaris, N.A., Tsirka, V., Vourkas, M., Micheloyannis, S., 2012b. Surface EEG shows that Functional Segregation via Phase Coupling contributes to the neural Substrate of Mental Calculations. Brain and Cognition, 80(1), 45–52.

Dimitriadis, S.I., Laskaris, N.A., Del Rio-Portilla, Y., Koudounis, G.C., 2009. Characterizing dynamic functional connectivity across sleep stages from EEG. Brain Topography, 22, 119-133.

Dimitriadis, S.I., Laskaris, N.A., Micheloyannis S., 2015. Dynamics of EEG-based Network Microstates unmask developmental and task differences during mental arithmetic and resting wakefulness. In Press in Cognitive Neurodynamics.

Dimitriadis, S.I., Laskaris, N.A., Simos, P.G., Micheloyannis, S., Fletcher, J.M., Rezaie, R., Papanicolaou, A.C., 2013b. Altered temporal correlations in resting-state connectivity fluctuations in children with reading difficulties detected via MEG. Neuroimage 83, 307–317.

Dimitriadis, S.I., Laskaris, N.A., Tsirka, V., Vourkas, M., Micheloyannis, S., Fotopoulos, S., 2010a. Tracking brain dynamics via time-dependent network analysis. Journal of Neuroscience Methods 193(1), 145-155.

Dimitriadis, S.I., Laskaris, N.A., Tsirka, V., Vourkas, M., Micheloyannis, S., 2010b. What does delta band tell us about cognitive Processes: a mental calculation study? Neuroscience Letters 483 (1), 11-15.

Dimitriadis, S.I., Laskaris, N.A., Tsirka, V., Vourkas, M., Micheloyannis, S. 2012a. An EEG study of brain connectivity dynamics at the resting state. Nonlinear Dynamics, Psychology and Life Sciences 16(1), 5-22.

Dimitriadis, S.I., Laskaris, N.A., Tzelepi A., 2013a. On the quantization of time-varying phase synchrony patterns into distinct Functional Connectivity Microstates (FCµstates) in a multi-trial visual ERP paradigm, (3), 397-409.

Dimitriadis, S.I., Laskaris, N.A., Tzelepi, A., Economou, G., 2012c. Analyzing Functional Brain Connectivity by means of Commute Times: a new approach and its application to track event-related dynamics. IEEE (TBE) Transactions on Biomedical Engineering, 59(5), 1302-1309.

Dimitriadis, S.I., Sun, Yu, Kwok K., Laskaris, N.A., Thakor, N., Bezerianos, A., 2014. Cognitive Workload Assessment Based on the Tensorial Treatment of EEG Estimates of Cross-Frequency Phase Interactions. Annals of Biomedical Engineering October.

Douw, L., Baayen, H., Bosma, I., Klein, M., Vandertop, P., Heimans, J., et al., 2008. Treatment-related changes in functional connectivity in brain tumor patients: a magnetoencephalography study. Exp. Neurol. 212, 285–290.

Eierud, C, Craddock, R.C., Fletcher, S, 2014. Neuroimaging after mildtraumatic brain injury: review andmeta-analysis. Neuroimage Clin. 4, 283–94.

Engel, A.K., and Fries, P., 2010. Beta-band oscillations—signalling the status quo? Curr. Opin. Neurobiol. 20, 156–165.

Engel, A.K., Fries, P., and Singer, W., 2001. Dynamic predictions: oscillations and synchrony in top-down processing. Nat. Rev. Neurosci. 2, 704–716.

Engel, A.K., Gerloff, C., Hilgetag, C.C., Nolte, G., 2013. Intrinsic coupling modes: multiscale interactions in ongoing brain activity. Neuron 80, 867–886.

Escudero, J., Hornero, R., Abásolo, D., Fernández, A., 2011: Quantitative evaluation of artifact removal in real magnetoencephalogram signals with blind source separation. Ann Biomed Eng 39(8), 2274-86.

Florin, E, Baillet, S, 2015. The brain's resting-state activity is shaped by synchronized cross-frequency coupling of neural oscillations. Neuroimage, 111, 26-35.

Fornito A, Zalesky A, Pantelis C, Bullmore ET, (2012). Schizophrenia, neuroimaging and connectomics. Neuroimage 62(4):2296-2314.

Friston, K.J., Tononi, G., Reeke Jr., G.N., Sporns, O., Edelman, G.M., 1994. Value dependent selection in the brain: simulation in a synthetic neural model. Neuroscience 59 (2), 229–243.

Gallos, L.K., Cohen, R., Liljeros, F., Argyrakis, P., Bunde, A., and Havlin, S. (2006). Attack Strategies on Complex Networks, workshop on "Networks: structure and dynamics" in ICCS 2006, Lecture Notes in Computer Science 3993, 1048.

Gerloff, C., Bushara, K., Sailer, A., Wassermann, E.M., Chen, R., Matsuoka, T., Waldvogel, D., Wittenberg, G.F., Ishii, K., Cohen, L.G., Hallett, M., 2006. Multimodal imaging of

brain reorganization in motor areas of the contralesional hemisphere of well recovered patients after capsular stroke. Brain 129 (Pt 3), 791–808.

Gibbons, J.D. and Chakraborti, S., 2011: Nonparametric Statistical Inference, 5th Ed., Boca Raton, FL: Chapman & Hall/CRC Press, Taylor & Francis Group.

Girvan, M. and Newman, M.E.J., 2002 Proc. Natl. Acad. Sci. USA 99 7821.

Han, K., Mac Donald C. L., Johnson A. M., Barnes Y., Wierzechowski L., Zonies D., Oh J., Flaherty S., Fang R., Raichle M. E., Brody D. L., 2014. Disrupted modular organization of resting-state cortical functional connectivity in U.S. military personnel following concussive 'mild' blast-related traumatic brain injury. NeuroImage 84, 76-96.

He X, Cai D, Niyogi P. Laplacian score for feature selection. In Advances in Neural Information Processing Systems 18 Weiss, Scholkopf, Platt (editors). MIT Press, Cambridge, MA, 2005.

He, Y. and Evans, A., 2010. Graph theoretical modeling of brain connectivity. Current opinion in neurology 23(4), 341-350.

Hipp, J.F., Hawellek, D.J., Corbetta, M., Siegel, M., and Engel, A.K., 2012. Large-scale cortical correlation structure of spontaneous oscillatory activity. Nat. Neurosci. 15, 884–890.

Ho, T.K., 1998. The random subspace method for constructing decision forests. IEEE Trans. on Pattern Analysis and Machine Intelligence, 20 (8), 832–844.

Huang G.-B., and Chen, L., "Convex incremental extreme learning machine," Neurocomputing, vol. 70, nos. 16–18, pp. 3056–3062, 2007.

Huang G.-B., and Chen, L., "Enhanced random search based incremental extreme learning machine," Neurocomputing, vol. 71, nos. 16–18, pp. 3460–3468, 2008

Huang, D., Yang, B., Tan, B., Rautiainen, M., Zhang, P., Hu, J., Shabanov, N.V., Linder, S., Knyazikhin, Y., Myneni, R.B., 2006. The importance of measurement errors for deriving accurate reference leaf area index maps for validation of moderate-resolution satellite LAI products. IEEE Transactions on Geoscience and Remote Sensing.

Huang, et al., 2014. Single-subject-based whole-brain MEG slow-wave imaging approach for detecting abnormality in patients with mild traumatic brain injury. NeuroImage: Clinical 5, 109–119.

Huang, G.-B., "An insight into extreme learning machines: Random neurons, random features and kernels," Cognit. Comput., vol. 6, no. 3, pp. 376–390, 2014

Huang, G.-B., Chen, L., and Siew, C.-K., "Universal approximation using incremental constructive feedforward networks with random hidden nodes," IEEE Trans. Neural Netw., vol. 17, no. 4, pp. 879–892, Jul. 2006.

Huang, G.-B., Zhou, H., Ding, X. and Zhang, R.,"Extreme learning machine for regression and multiclass classification," IEEE Trans. Syst., Man, Cybern. B, Cybern., vol. 42, no. 2, pp. 513–529, Apr. 2012.

Huang, M.X., Theilmann, R.J., Robb, A., Angeles, A.,Nichols, S.,Drake, A., D'Andrea, J., Levy,M., Holland, M., Song, T., Ge, S., Hwang, E., Yoo, K., Cui, L., Baker, D.G., Trauner, D., Coimbra, R., Lee, R.R., 2009. Integrated imaging approach with MEG and DTI to detect mild traumatic brain injury in military and civilian patients. J. Neurotrauma 26, 1213–1226.

Jensen, O., and Colgin, L.L., 2007. Cross-frequency coupling between neuronal oscillations. Trends Cogn. Sci. 11, 267–269.

Jeter, C.B., Hergenroeder, G.W., Hylin, M.J., Redell, J.B., Moore, A.N., Dash, P.K., 2013. Biomarkers for the diagnosis and prognosis of mild traumatic brain injury/concussion. J. Neurotrauma 30, 657–670.

Jirsa, V, Müller V, 2013. Cross-frequency coupling in real and virtual brain networks. Front Comput Neurosci., 7:78.

Johnston, K.M., Ptito, A., Chankowsky, J., Chen, J.K., 2001. New frontiers in diagnostic imaging in concussive head injury. Clin. J. Sport Med. 11, 166–175.

Kay, T., Harrington, D.E., Adams, R., Anderson, T., Berrol, S., Cicerone, K., Dahlberg, C., Gerber, D., Goka, R., Harley, P., Hilt, J., Horn, L., Lehmkuhl, D., Malec, J., 1993. Definition of mild traumatic brain injury. J. Head Trauma Rehabil. 8, 86–87.

Kirkwood, M.W., Yeates, K.O., Wilson, P.E., 2006. Pediatric sport-related concussion: a review of the clinical management of an oft-neglected population. Pediatrics 117, 1359–1371.

Kolchinsky, A., Van Den Heuvel, M.P., Griffa, A., Hagmann, P., Rocha Luis, M., Sporns O., Goni, J., 2014. Multi-scale Integration and Predictability in Resting State Brain Activity, Front Neuroinf 8, 66.

Kramer, M.A. et al., 2008. Sharp edge artifacts and spurious coupling in EEG frequency comodulation measures. J. Neurosci. Methods 170, 352–357.

Kuncheva, L.I., Rodriguez, J.J., Plumpton, C.O., Linden, D.E., Johnston, S.J., 2010. Random subspace ensembles for FMRI classification, IEEE Transaction on Medical Imaging, 29(2), 531–542.

Lakatos, P. et al., 2005. An oscillatory hierarchy controlling neuronal excitability and stimulus processing in the auditory cortex. J. Neurophysiol. 94, 1904–1911.

Laskaris, N.A., Tarnanas, I., Tsolaki, M.N., Vlaikidis, N., and Karlovasitou, A.K.(2013).Improved detection of amnestic MCI by means of discriminative vector quantization of single-trial cognitive ERP responses. J Neurosci Methods. 30;212(2),344-354.

Latchoumane, C. F., F. B. Vialatte, J. Sole-Casals, M. Maurice, S. R. Wimalaratna, N. Hudson, J. Jeong, and A. Cichocki. Multiway array decomposition analysis of EEGs in Alzheimer's disease. J. Neurosci. Methods 207:41–50, 2012.

Leahy, R.M., Mosher, J.C., Spencer, M.E., Huang, M.X., Lewine, J.D., 1998. A study of dipole localization accuracy for MEG and EEG using a human skull phantom. Electroencephalogr. Clin. Neurophysiol. 107, 159–173.

Leonardi, N., and D. Van de Ville. Identifying network correlates of brain states using tensor decompositions of whole-brain dynamic functional connectivity. In: International Workshop on Pattern Recognition in Neuroimaging (PRNI), 2013, pp. 74–77.

Leuchter, A.F., Cook, I.A., Newton, T.F., Dunkin, J., Walter, D.O., Rosenberg-Thompson, S., Lachenbruch, P.A, and Weiner, H., 1993. Regional differences in brain electrical activity in dementia: use of spectral power and ratio measures Electroencephalogr. Clin. Neurophysiol. 87 385–93.

Levin, H.S., 2009. Mission Connect Mild TBI Translational Research Consortium. Baylor College of Medicine Houston TX.

Levin, H.S., Mattis, S., Ruff, R.M., Eisenberg, H.M., Marshall, L.F., Tabaddor, K., High, Jr. W.M., Frankowski R.F., 1987. Neurobehavioral outcome following minor head injury: a three-center study. J. Neurosurg. 66, 234–243.

Levin, H.S., O'Donnell, V.M., Grossman, R.G., 1979. The Galveston Orientation and Amnesia Test. A practical scale to assess cognition after head injury. J Nerv Ment Dis. 167(11), 675-84.

Levine, B., Cabeza, R., McIntosh, A.R., Black, S.E., Grady, C.L., Stuss, D.T., 2002. Functional reorganisation of memory after traumatic brain injury: a study with H2150 positron emission tomography. J Neurol Neurosurg Psychiatry 73, 173-181.

Li, L., Pagnotta, M.F., Arakaki, X., Tran, T., Strickland, D., Harrington M., and, Zouridakis G., 2015. Brain Activation Profiles in mTBI: Evidence from Combined Resting-State EEG and MEG Activity, Conf Proc IEEE Eng Med Biol Soc., August 25-29, 2015, accepted.

Liu, Y, Liang, M, Zhou, Y, et al (2008). Disrupted small-world networks in schizophrenia. Brain. 131(pt 4):945-961.

Luo, Q., Xu, D., Roskos, T., Stout, J., Kull, L., Cheng, X., Whitson, D., Boomgarden, E., Gfeller, J., Bucholz, R.D., 2013. Complexity analysis of resting state magnetoencephalography activity in traumatic brain injury patients. J. Neurotrauma 30, 1702–1709.

Meilă, M., 2007. Comparing clusterings—an information based distance. J. of Multivar. Anal. 98(5), 873-895.

Minhas, R., Baradarani, A., Seifzadeh, S., and Wu, Q. M. J., "Human action recognition using extreme learning machine based on visual vocabularies," Neurocomputing, vol. 73, nos. 10–12, pp. 1906–1917, 2010.

Mišić, B., Sporns, O., McIntosh, A.R. 2014. Communication Efficiency and Congestion of Signal Traffic in Large-Scale Brain Networks. PLoS Comput Biol 10(1):e1003427..

Mohammed, A. A., Minhas, R., Wu, Q. M. J., and Sid-Ahmed, M. A., "Human face recognition based on multidimensional PCA and extreme learning machine," Pattern Recognit., vol. 44, nos. 10–11, pp. 2588–2597, 2011.

National Institute on Aging. *Alzheimer 's disease. Unraveling the Mystery,* volume 08-3782 of the National Institute of Health (NIH) Publication. U.S. Department of Health and Human Services, 2008.

Newman, M.E.J., 2006 Proc. Natl. Acad. Sci. USA 103 8577.

Oostenveld, R., Fries, P., Maris E., Schoelen, J.M., 2011. Fieldtrip: Open source software for advanced analysis of meg, eeg, and invasive electrophysiological data. Computational Intelligence and Neuroscience 2011 (Article ID 156869), 9 pages.

Osipova, D., Hermes, D., and Jensen, O., 2008. Gamma power is phase-locked to posterior alpha activity. *PLoSONE* 3, 7.

Palva, J.M. et al., 2005. Phase synchrony among neuronal oscillations in the human cortex. J. Neurosci. 25, 3962–3972.

Palva, J.M., and Palva, S., 2011. Roles of multiscale brain activity fluctuations in shaping the variability and dynamics of psychophysical performance. Prog. Brain Res. 193, 335– 350.

Pan, C., Park, D. S., Yang, Y., and Yoo, H. M., "Leukocyte image segmentation by visual attention and extreme learning machine," Neural Comput. Appl., vol. 21, no. 6, pp. 1217–1227, 2012.

Penny, W.D. et al. (2008) Testing for nested oscillation. J. Neurosci. Methods 174, 50–61.

Pinal, D., Zurróna, M., Díaza, F, Sauseng, P., 2015. Stuck in default mode: inefficient cross-frequency synchronization may lead to age-related short-term memory decline. Neurobiology of aging.

Rapp, P. E., Keyser, D. O., Albano, A., Hernandez, R., Gibson, D. B., Zambon, R. A., … Nichols, A. S. (2015). Traumatic Brain Injury Detection Using Electrophysiological Methods. Frontiers in Human Neuroscience, 9, 11.

Raskin, S.A., 2000. Memory. In: Raskin, S.A., Mateer, C.A. (Eds.), Neuropsychological Management of Mild Traumatic Brain Injury. Oxford University Press, New York, 93– 107.

Reuter-Lorenz, P.A., Jonides, J., Smith, E.E., et al., 2000. Age differences in the frontal lateralization of verbal and spatial working memory revealed by PET. J. Cogn. Neurosci. 12, 174–87.

Richiardi, J., Eryilmaz, H., Schwartz, S., Vuilleumier, P., Van De Ville D., 2011. Decoding brain states from fMRI connectivity graphs. Neuroimage 56(2), 616-626.

Rodriguez G, Copello F, Vitali P, Perego G and Nobili F 1999 EEG spectral profile to stage Alzheimer's disease Clin.Neurophysiol. 110, 1831–7.

Rohling, M. L., Binder, L. M., Demakis, G. J., Larrabee, G. J., Ploetz, D. M., & Langhinrichsen-Rohling, J., 2011. A meta-analysis of neuropsychological outcome after mild traumatic brain injury: re-analyses and reconsiderations of Binder et al. (1997), Frencham et al. (2005), and Pertab et al. (2009). The Clinical Neuropsychologist, 25(4), 608– 623.

Rubinov M, Knock S, Stam C, Micheloyannis S, Harris A, et al. (2009) Small world properties of nonlinear brain activity in schizophrenia. Hum Brain Mapp30: 403–416.

Rubinov M, Sporns, O, 2010. Complex network measures of brain connectivity: Uses and interpretations. NeuroImage, 52, 1059-69.

Ruff, R.M., Levin, H.S., Mattis, S., High Jr., W.M., Marshall, L.F., Eisenberg, H.M., Tabaddor, K., 1989. Recovery of memory after mild head injury: a three-center study. In: Levin, H.S., Eisenberg, H.M., Benton, A.L. (Eds.), Mild Head Injury. Oxford University Press, New York, 176–188.

Sanei S., and Chambers J., 2007. EEG Signal Processing. Wiley-Interscience, Cichester, UK.

Scheeringa, R., Bastiaansen, M.C.M., Petersson, K.M., Oostenveld, R., Norris, D.G., Hagoort., P., 2008. Frontal theta EEG activity correlates negatively with the default mode network in resting state. Int. J. Psychophysiol., 67, 242–251.

Schroeter MS, Charlesworth P, Kitzbichler MG, Paulsen O, Bullmore ET, (2015). Emergence of rich-club topology and coordinated dynamics in development of hippocampal functional networks in vitro. J Neurosci. 8;35(14):5459-70.

Schutter, D. J. L. G., & Knyazev, G. G. (2012). Cross-frequency coupling of brain oscillations in studying motivation and emotion. Motivation and Emotion,36(1), 46–54.

Senden, M., Deco, G., de Reus, M. A., Goebel, R., van den Heuvel, M. P., 2014. Rich club organization supports a diverse set of functional network configurations. Neuro Im., 96:174-182.

Shen, H., Wang, L., Liu, Y., Hu, D., 2010. Discriminative analysis of resting-state functional connectivity patterns of schizophrenia using low dimensional embedding of fMRI. Neuroimage 49(4), 3110-3121.

Siegel, M., Donner, T.H., and Engel, A.K., 2012. Spectral fingerprints of largescale neuronal interactions. Nat. Rev. Neurosci. 13, 121–134.

Sigurdardottir, S., Andelic, N., Roe, C., Jerstad, T., Schanke, A.K., 2009. Post-concussion symptoms after traumatic brain injury at 3 and 12 months post-injury: a prospective study. Brain Injury 23(6), 489-497.

Skurichina, M., 2002. Bagging, boosting and the random subspace method for linear classifiers. Pattern Analysis and Applications 5(2), 121–135.

Stam, C.J., 2010. Characterization of anatomical and functional connectivity in the brain: a complex networks perspective. International Journal of Psychophysiology 77(3), 186-194.

Steriade, M., Amzica, F., and Contreras, D. 1996a. Synchronization of fast (30-40 Hz) spontaneous cortical rhythms during brain activation. J. Neurosci. 16, 392–417.

Steriade, M., Contreras, D., Amzica, F., and Timofeev, I. (1996b). Synchronization of fast (30-40 Hz) spontaneous oscillations in intrathalamic and thalamocortical networks. J. Neurosci. 16, 2788–2808.

Teasdale, G., Jennett, B., 1974. Assessment of coma and impaired consciousness. A practical scale. Lancet. 2(7872), 81-4.

Tognoli, G., and Scott Kelso, J.A, 2014b. The Metastable Brain.

Tognoli, G., and Scott Kelso, J.A., 2014a.Enlarging the scope: grasping brain complexity. Frontiers of Systems Neuroscience.

Tononi, G., Sporns, O., and Edelman, G.M., 1994. A measure for brain complexity: relating functional segregation and integration in the nervous system. *Proc. Natl. Acad. Sci. USA* 91, 5033–5037.

Tort, A.B.L., Komorowski, R., Eichenbaum, H., and Kopell, N., 2010. Measuring phase-amplitude coupling between neuronal oscillations of different frequencies. *J. Neurophysiol.* 104, 1195–1210.

Tort, A.B.L., Komorowski, R.W., Manns, J.R., Kopell, N.J., and Eichenbaum, H., 2009. Theta–gamma coupling increases during the learning of item–context associations. *Proc. Natl. Acad. Sci. U.S.A.* 106, 20942–20947.

Tort, A.B.L., Kramer, M.A., Thorn, C., Gibson, D. J., Kubota, Y., Graybiel, A. M., 2008. Dynamic cross-frequency couplings of local field potential oscillations in ratstriatum and hippocampus during performance of aT-mazetask. *Proc.Natl.Acad.Sci.U.S.A.* 105, 20517–20522.

Tsiaras, V., Simos, P.G., Rezaie, R., Sheth, B.R., Garyfallidis, E., Castillo, E.M., et al., 2011. Extracting biomarkers of autism from MEG resting-state functional connectivity networks. Comput. Biol. Med. 41, 1166–1177.

Tsirka, V, Simos, P.G, Vakis, A., Kanatsouli, K., Vourkas, M., Erimaki, S., Pachou, E., Stam, C.J., Micheloyannis, S., 2011. Mild traumatic brain injury: Graph-model characterization of brain networks for episodic memory. Int. J. of Psychophysiol. 79, 89–96.

Van den Heuvel MP, Sporns O. J, (2011). Rich-club organization of the human connectome. Neurosci. 31(44):15775-86.

van den Heuvel MP, Kahn RS, (2011). Abnormal brain wiring as a pathogenetic mechanism in schizophrenia. Biol Psychiatry 70(12):1107-1108.

Van den Heuvel MP, Sporns O, Collin G, et al. Abnormal Rich Club Organization and Functional Brain Dynamics in Schizophrenia. JAMA Psychiatry.2013;70(8):783-792.

Vanderploeg, R.D., Curtiss, G., Belanger, H.G., 2005. Long-term neuropsychological outcomes following mild traumatic brain injury. J. Int. Neuropsychol. Soc. 11, 228–236.

Voytek, B., Canolty, R.T., Shestyuk, A., Crone, N. E., Parvizi, J., Knight, R. T., 2010. Shifts in Gamma Phase–Amplitude Coupling Frequency from Theta to Alpha Over Posterior Cortex During Visual Tasks. Front. Hum. Neurosci. 4, 191.

Vértes PE, Bullmore ET., (2015). Annual research review: Growth connectomics--the organization and reorganization of brain networks during normal and abnormal development. J Child Psychol Psychiatry. 56(3):299-320.

Watts DJ, Strogatz SH., (1998). Collective dynamics of 'small-world' networks. Nature. 4; 393(6684):440-2.

Xu, X., Zheng, C., & Zhang, T., 2013. Reduction in LFP cross-frequency coupling between theta and gamma rhythms associated with impaired STP and LTP in a rat model of brain ischemia. Frontiers in Computational Neuroscience, 7, 27.

Young, C.K. and Eggermont, J.J., 2009. Coupling of mesoscopic brain oscillations: recent advances in analytical and theoretical perspectives. Prog. Neurobiol. 89, 61–78.

Zouridakis, G., Paditar, U., Situ, N., Rezaie, R., Castillo, E., Levin, H., Papanicolaou, A.C., 2012. Functional Connectivity Changes in Mild Traumatic Brain Injury Assessed Using Magnetoencephalography. J of Mechanics in Medicine and Biology 12(02).

Publications

Conferences

1. **M. Antonakakis**, G. Giannakakis, M. Tsiknakis, S. Micheloyannis and M Zervakis. Synchronization coupling investigation using ICA cluster analysis in resting MEG signals in Reading Difficulties. In Proceedings of the IEEE 13th International Conference on Bioinformatics and Bioengineering (BIBE), November 10-13, 2013.

2. **M. Antonakakis**, V. Tsirka, M. Zervakis and S. Micheloyannis (2014): A Minimal Spanning Tree Analysis of EEG Responses to Complex Visual Stimuli. 26th IEEE International Conference on Tools with Artificial Intelligence (ICTAI), Limassol, Cyprus, November 10-12, 2014.

3. **M. Antonakakis,** Tsirka V, S. I. Dimitriadis, S. Micheloyannis and M. Zervakis. Rich Club Differentiation of Phase Synchronization EEG Responses. 6th PANHELLENIC CONFERENCE ON BIOMEDICAL TECHNOLOGY (ELEVIT), Athens, Greece, May 6-8, 2015.

4. **M. Antonakakis**, S. I. Dimitriadis, M. Zervakis, R. Rezaie, A. Babajani-Feremi, S. Micheloyannis and A. C. Papanicolaou. Uncovering the brain model of MEG Brain Networks from Cross-Frequency Coupling Estimates via an attacking strategy. 37TH ANNUAL INTERNATIONAL CONFERENCE OF THE IEEE Engineering in Medicine and Biology Society (EMBC), Milan, Italy, August 25-29 2015.

Journals

1. **M. Antonakakis**, S. I. Dimitriadis, M. Zervakis , R. Rezaie, Abbas Babajani-Feremi, S. Micheloyannis and A. C. Papanicolaou. Detect Mild Traumatic Brain Injury from Resting-state MEG recordings based on Cross-frequency Interactions (Submitted on International Journal of Psychophysiology), July 2015.

2. **M. Antonakakis**, S. I. Dimitriadis, M. Zervakis, R. Rezaie, A. Babajani-Feremi, S. Micheloyannis and A. C. Papanicolaou. Mind network models: A Comparative Study of small-world and rich-club architectures of Cross-frequency brain networks in mild Traumatic Brain Injury during Resting-state MEG recordings. In Preparation for Brain Connectivity Journal.